

# Multiple-Parameter Graph Fractional Fourier Transform: Theory and Applications

Manjun Cui, Zhichao Zhang, *Member, IEEE*, and Wei Yao

**Abstract**—The graph fractional Fourier transform (GFRFT) applies a single global fractional order to all graph frequencies, which restricts its adaptability to diverse signal characteristics across the spectral domain. To address this limitation, in this paper, we propose two types of multiple-parameter GFRFTs (MPGFRFTs) and establish their corresponding theoretical frameworks. We design a spectral compression strategy tailored for ultra-low compression ratios, effectively preserving essential information even under extreme dimensionality reduction. To enhance flexibility, we introduce a learnable order vector scheme that enables adaptive compression and denoising, demonstrating strong performance on both graph signals and images. We explore the application of MPGFRFTs to image encryption and decryption. Experimental results validate the versatility and superior performance of the proposed MPGFRFT framework across various graph signal processing tasks.

**Index Terms**—multiple-parameter graph fractional Fourier transform, learnable order vector, spectral compression, denoising.

## I. INTRODUCTION

Graph signal processing (GSP) is an emerging framework that generalizes classical signal processing (SP) techniques to data defined on irregular domains modeled by graphs [1]–[4]. It provides powerful tools for analyzing and manipulating signals that reside on the nodes of a graph, where the underlying structure encodes complex relationships between data elements. GSP has been widely applied in a variety of fields, including classification, filtering, spectral analysis, social network analysis, and image processing, and so on [2], [5]–[12].

A cornerstone of GSP is the graph Fourier transform (GFT) [7], [8], [13]–[16], which extends the classical Fourier transform (FT) [17], [18] to graph-structured data by projecting signals onto the eigenbasis of a graph shift operator (GSO) [7], [19]–[24], such as the graph Laplacian or adjacency matrix. While the GFT enables spectral analysis on graphs, it lacks the ability to explore intermediate representations

between the vertex and frequency domains. To address this limitation, Wang et al. [25] first proposed the graph fractional Fourier transform (GFRFT), which introduces a fractional order parameter to interpolate between the identity transform and the full GFT. In this formulation, the GFRFT is defined by applying a fractional power of the GFT matrix derived from a given GSO, thereby extending the core idea of the classical fractional Fourier transform (FRFT) [26], [27] to graph domains via spectral-domain modulation. Subsequent works have further developed the GFRFT framework by extending it along multiple directions [28]–[32]. More recently, a hyper-differential operator-based GFRFT has been introduced in [33], which generalizes the notion of fractional powers and ensures differentiability with respect to the order parameter. This advancement is significant as it enables gradient-based learning of the fractional order parameter within task-specific optimization pipelines. As a result, the transform becomes not only flexible but also learnable, allowing it to adapt to data-driven objectives in applications. Building on these foundations, researchers have explored the application of GFRFT in various graph signal processing tasks. For instance, in graph signal denoising, intermediate-domain representations can suppress noise while preserving essential structures, especially when noise is spectrally localized [28], [31], [33]–[35]. In data compression, GFRFT enables better energy compaction and sparsity by concentrating signal energy in fractional spectral bases [36], [37]. Moreover, GFRFT has also been explored in graph signal filtering, its integration into graph neural networks, and a variety of other graph-based learning scenarios [38]–[40]. Despite these developments, existing GFRFT frameworks share a fundamental limitation that the fractional order parameter is uniformly applied to all spectral components. This assumption may not hold in practice, as high-frequency components often capture noise or small-scale structure, while low-frequency components encode coarse, global features.

In SP, similar limitations of the FRFT have been addressed through the development of multiple-parameter discrete FRFTs (MPDFRFTs). Pei and Hsue [41] introduced the MPDFRFT by applying distinct fractional powers to the eigenvalues of the discrete Fourier transform (DFT) matrix, thereby allowing frequency components to be modulated individually. Building upon this foundation, Kang et al. [42] proposed two generalized forms of MPDFRFT and developed a unified theoretical framework, enabling broader applications in SP. MPDFRFTs have been applied to image encryption and decryption, where frequency-dependent modulation provides enhanced security through increased key space and spectral

This work was supported in part by the Open Foundation of Hubei Key Laboratory of Applied Mathematics (Hubei University) under Grant HBAM202404; and in part by the Foundation of Key Laboratory of System Control and Information Processing, Ministry of Education under Grant Scip20240121. (*Corresponding author: Zhichao Zhang.*)

Manjun Cui and Wei Yao are with the School of Mathematics and Statistics, Nanjing University of Information Science and Technology, Nanjing 210044, China (e-mail: cmj1109@163.com; yaowei@nuist.edu.cn).

Zhichao Zhang is with the School of Mathematics and Statistics, Nanjing University of Information Science and Technology, Nanjing 210044, China, with the Hubei Key Laboratory of Applied Mathematics, Hubei University, Wuhan 430062, China, and also with the Key Laboratory of System Control and Information Processing, Ministry of Education, Shanghai Jiao Tong University, Shanghai 200240, China (e-mail: zzc910731@163.com).

diversity. These advances have proven effective in a variety of signal processing and information security applications. Inspired by this idea, we extend the concept of MPDFRFT to the graph domain and propose the multiple-parameter GFRFTs (MPGFRFTs), enabling each graph frequency to be individually modulated by a dedicated order parameter. This framework offers greater flexibility and exhibits strong potential across various applications. By adapting the spectral representation to the characteristics of graph signals, the MPGFRFT can be effectively applied to compression, denoising, and graph-based image encryption and decryption.

The main contributions of this paper are summarized as follows:

- We propose two types of MPGFRFTs and establish their corresponding theoretical frameworks.
- We introduce a novel spectral compression strategy tailored for ultra-low compression ratios.
- We develop both transform learning and order vector learning schemes within the MPGFRFT framework. Building upon order vector learning, we further propose a learnable compression method that adapts to signal characteristics.
- MPGFRFT is effectively applied to graph signal denoising. The framework supports graph-based image encryption and decryption.

The remainder of this paper is organized as follows. Section II provides the necessary preliminaries. Section III introduces the definition and theoretical properties of the proposed MPGFRFTs, and further develops a learnable order vector scheme under this framework. Section IV presents a novel spectral compression strategy tailored for ultra-low compression ratios. Section V provides some applications within the MPGFRFT framework. Finally, Section VI concludes the paper. Fig. 1 outlines the MPGFRFTs' development, theoretical foundation, and applications. All the technical proofs of our theoretical results are relegated to the Appendix parts.

## II. PRELIMINARIES

### A. Graph Fourier Transform

Let  $\mathcal{G} = \{\mathcal{N}, \mathcal{E}, \mathbf{A}\}$  be a graph or network with node set  $\mathcal{N}$ , edge set  $\mathcal{E}$  and adjacency matrix  $\mathbf{A} \in \mathbb{R}^{N \times N}$ . The weighted adjacency matrix  $\mathbf{W}$  encodes edge weights, where  $W_{mn}$  quantifies the strength of the connection between nodes  $m$  and  $n$ , and all diagonal elements satisfy  $W_{nn} = 0$ . The Laplacian is defined as  $\mathbf{L} = \mathbf{D} - \mathbf{W}$ , where  $\mathbf{D}$  is the diagonal degree matrix with  $D_{nn} = \sum_{m=1}^N W_{nm}$ . In GSP, the general GSO  $\mathbf{Z}$  plays a central role in defining spectral transforms. Typical choices for the GSO include the adjacency matrix  $\mathbf{A}$ , the weighted adjacency matrix  $\mathbf{W}$ , the Laplacian  $\mathbf{L}$ , or their normalized variants. Let the Jordan decomposition of the GSO be written as  $\mathbf{Z} = \mathbf{P}_Z \mathbf{J}_Z \mathbf{P}_Z^{-1}$ , where  $\mathbf{J}_Z$  is the Jordan block matrix. In particular, if  $\mathbf{Z}$  is diagonalizable, it admits the eigendecomposition  $\mathbf{Z} = \mathbf{U} \mathbf{\Lambda} \mathbf{U}^{-1}$ , where  $\mathbf{U}$  consists of the eigenvectors of  $\mathbf{Z}$  and  $\mathbf{\Lambda}$  is a diagonal matrix of eigenvalues. Unless otherwise stated, we assume throughout this paper that the GSO is diagonalizable. A graph signal is defined as a

function  $\mathbf{x} : \mathcal{N} \rightarrow \mathbb{C}$ , which can be represented as a vector  $\mathbf{x} = [x(1), x(2), \dots, x(N)]^T \in \mathbb{C}^N$ .

The GFT of a signal  $\mathbf{x}$  is defined as

$$\hat{\mathbf{x}} = \mathbf{F} \mathbf{x} = \mathbf{U}^{-1} \mathbf{x}, \quad (1)$$

where  $\mathbf{F} = \mathbf{U}^{-1}$  is the GFT matrix. The inverse GFT is given by

$$\mathbf{x} = \mathbf{F}^{-1} \hat{\mathbf{x}} = \mathbf{U} \hat{\mathbf{x}}. \quad (2)$$

### B. Graph Fractional Fourier Transform

Suppose that the GFT matrix  $\mathbf{F}$  is diagonalizable, the eigendecomposition of  $\mathbf{F}$  is

$$\mathbf{F} = \mathbf{V} \mathbf{\Lambda}_F \mathbf{V}^{-1}, \quad (3)$$

where  $\mathbf{\Lambda}_F = \text{diag}(\lambda_0, \lambda_1, \dots, \lambda_{N-1})$  a diagonal matrix of eigenvalues and  $\mathbf{V} = [\mathbf{v}_0, \mathbf{v}_1, \dots, \mathbf{v}_{N-1}]$  is the matrix whose columns are the corresponding eigenvectors of  $\mathbf{F}$ . In this paper, we assume that the eigenvalues are distinct. Then, the GFRFT matrix of order  $a$  is defined as

$$\mathbf{F}^a = \mathbf{V} \mathbf{\Lambda}_F^a \mathbf{V}^{-1}, \quad (4)$$

where  $\mathbf{\Lambda}_F^a = \text{diag}(\lambda_0^a, \lambda_1^a, \dots, \lambda_{N-1}^a)$ . Thus, the GFRFT of a signal  $\mathbf{x}$  is given by [43]

$$\hat{\mathbf{x}}_a = \mathbf{F}^a \mathbf{x}. \quad (5)$$

The GFRFT preserves the index additivity property, i.e.  $\mathbf{F}^a \mathbf{F}^b = \mathbf{F}^{a+b}$  for all  $a, b \in \mathbb{R}$ , which naturally enables the definition of the inverse transform

$$\mathbf{x} = (\mathbf{F}^a)^{-1} \hat{\mathbf{x}}_a. \quad (6)$$

Notably, the GFRFT reduces to the identity matrix when  $a = 0$ , i.e.,  $\mathbf{F}^0 = \mathbf{I}_N$ , and reduces to the GFT when  $a = 1$ , i.e.,  $\mathbf{F}^1 = \mathbf{F}$ .

## III. MULTIPLE-PARAMETER GRAPH FRACTIONAL FOURIER TRANSFORM

### A. Definitions

The GFRFT extends the GFT by introducing a fractional order parameter  $a$ , allowing spectral analysis to be performed in intermediate domains between the vertex and frequency representations. While GFRFT provides additional flexibility over GFT, it remains limited in that all spectral components are modulated using the same fractional order. However, different frequency components may exhibit varying degrees of importance or structure.

In SP, the MPDFRFT [41], [42] has been proposed to address similar limitations of single-parameter FRFT. Inspired by this, we extend the scalar order  $a$  to an order vector  $\mathbf{a} = (a_0, a_1, \dots, a_{N-1}) \in \mathbb{R}^N$  with  $N$  parameters, where each graph frequency component is assigned a distinct fractional order. This leads to the definition of the first type of MPGFRFT (MPGFRFT-I).

*Definition 1:* Given an order vector  $\mathbf{a} = (a_0, a_1, \dots, a_{N-1})$ , the MPGFRFT-I of signal  $\mathbf{x}$  is defined as

$$\hat{\mathbf{x}}_a^I = \mathbf{F}_I^a \mathbf{x}, \quad (7)$$

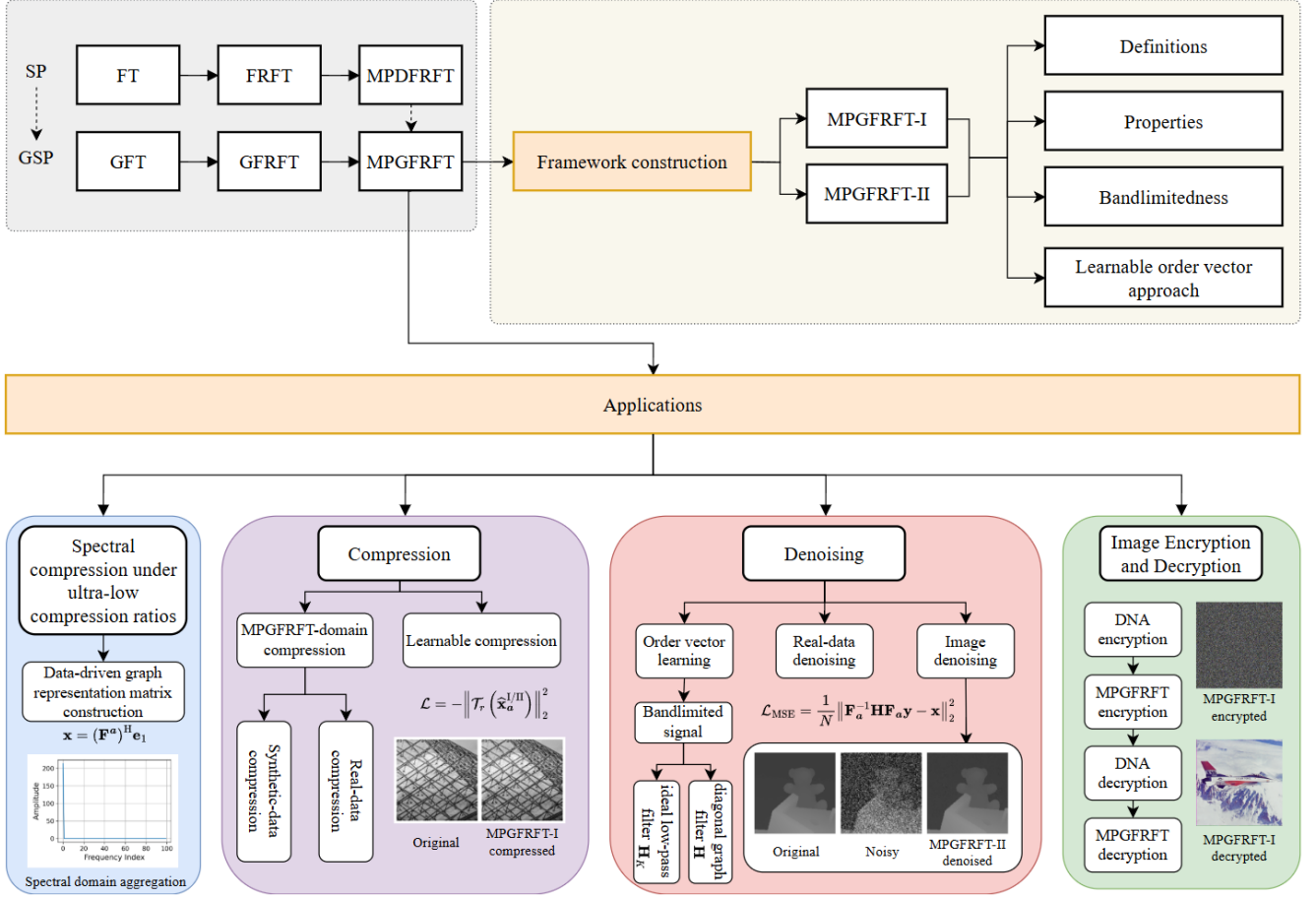


Fig. 1. Overview of the proposed MPGFRFT framework and its applications.

where  $\mathbf{F}_I^a$  denotes the MPGFRFT-I matrix, given by

$$\mathbf{F}_I^a = \mathbf{V} \mathbf{\Lambda}_F^a \mathbf{V}^{-1}, \quad (8)$$

with  $\mathbf{\Lambda}_F^a \triangleq \text{diag}(\lambda_0^{a_0}, \lambda_1^{a_1}, \dots, \lambda_{N-1}^{a_{N-1}})$ .

*Theorem 1:* Let  $\mathbf{a} = (a_0, a_1, \dots, a_{N-1})$  be any order vector, and let the eigenvalue matrix  $\mathbf{\Lambda}_F = \text{diag}(\lambda_0, \lambda_1, \dots, \lambda_{N-1})$  consist of pairwise distinct eigenvalues. The MPGFRFT-I matrix defined in (8) admits the following polynomial representation

$$\mathbf{F}_I^a = \sum_{n=0}^{N-1} C_{n,a_n}^I \mathbf{F}^n, \quad (9)$$

where the coefficient  $C_{n,a_n}^I$  is given by

$$C_{n,a_n}^I = \sum_{j=0}^{N-1} p_{n+1,j+1} \lambda_j^{a_j}, \quad (10)$$

and the matrix  $\mathbf{P} = (p_{ij})$  is defined as

$$\mathbf{P} = (p_{ij}) \triangleq \begin{pmatrix} 1 & \lambda_0 & \dots & \lambda_0^{N-1} \\ 1 & \lambda_1 & \dots & \lambda_1^{N-1} \\ \vdots & \vdots & \ddots & \vdots \\ 1 & \lambda_{N-1} & \dots & \lambda_{N-1}^{N-1} \end{pmatrix}^{-1}. \quad (11)$$

*Proof:* According to (8) and (9), we have

$$\mathbf{\Lambda}_F^a = \sum_{n=0}^{N-1} C_{n,a_n}^I \mathbf{\Lambda}_F^n, \quad (12)$$

which can be equivalently represented as a matrix-vector product

$$\begin{pmatrix} 1 & \lambda_0 & \dots & \lambda_0^{N-1} \\ 1 & \lambda_1 & \dots & \lambda_1^{N-1} \\ \vdots & \vdots & \ddots & \vdots \\ 1 & \lambda_{N-1} & \dots & \lambda_{N-1}^{N-1} \end{pmatrix} \begin{pmatrix} C_{0,a_0}^I \\ C_{0,a_1}^I \\ \vdots \\ C_{N-1,a_{N-1}}^I \end{pmatrix} = \begin{pmatrix} \lambda_0^{a_0} \\ \lambda_1^{a_1} \\ \vdots \\ \lambda_{N-1}^{a_{N-1}} \end{pmatrix}. \quad (13)$$

If the eigenvalues are distinct, the Vandermonde matrix is invertible, and we have

$$\begin{pmatrix} C_{0,a_0}^I \\ C_{0,a_1}^I \\ \vdots \\ C_{N-1,a_{N-1}}^I \end{pmatrix} = \mathbf{P} \begin{pmatrix} \lambda_0^{a_0} \\ \lambda_1^{a_1} \\ \vdots \\ \lambda_{N-1}^{a_{N-1}} \end{pmatrix}, \quad (14)$$

and therefore, we arrive the required result.  $\square$

Correspondingly, the second type of MPGFRFT (MPGFRFT-II) can be formulated by applying the fractional orders within the coefficient generation process of the matrix polynomial expansion.

**Definition 2:** Given an order vector  $\mathbf{a} = (a_0, a_1, \dots, a_{N-1})$ , the MPGFRFT-II of signal  $\mathbf{x}$  is defined as

$$\hat{\mathbf{x}}_{\mathbf{a}}^{\text{II}} = \mathbf{F}_{\text{II}}^{\mathbf{a}} \mathbf{x}, \quad (15)$$

where the MPGFRFT-II matrix  $\mathbf{F}_{\text{II}}$  is expressed as

$$\mathbf{F}_{\text{II}}^{\mathbf{a}} = \sum_{n=0}^{N-1} C_{n,a_n}^{\text{II}} \mathbf{F}^n, \quad (16)$$

with coefficients

$$C_{n,a_n}^{\text{II}} = \sum_{j=0}^{N-1} p_{n+1,j+1} \lambda_j^{a_n}. \quad (17)$$

**Remark 1:** When the underlying graph is a cycle graph, the MPGFRFT-I matrix degenerates to the MPDFRFT matrix proposed in [41]. Furthermore, if the matrix exhibits periodicity, MPGFRFT-I reduces to the type I MPDFRFT defined in [42]. Similarly, the MPGFRFT-II matrix reduces to the type II MPDFRFT in [42], since the GFT matrix of a cycle graph coincides with the DFT matrix. In this case, the coefficients  $C_{n,a_n}^{\text{II}}$  in (17) correspond to the  $(n+1)$ -th entry of the inverse DFT of  $\lambda^{a_n} = (\lambda_0^{a_n}, \lambda_1^{a_n}, \dots, \lambda_{N-1}^{a_n})^T$ , which matches the weight coefficients used in the type II MPDFRFT [42].

**Theorem 2:** Suppose the GSO is real and symmetric, the MPGFRFT-I matrix  $\mathbf{F}_{\text{I}}^{\mathbf{a}}$  is unitary for any order vector  $\mathbf{a}$ , that is,

$$\mathbf{F}_{\text{I}}^{\mathbf{a}} (\mathbf{F}_{\text{I}}^{\mathbf{a}})^{\text{H}} = (\mathbf{F}_{\text{I}}^{\mathbf{a}})^{\text{H}} \mathbf{F}_{\text{I}}^{\mathbf{a}} = \mathbf{I}_N. \quad (18)$$

**Proof:** If the GSO is real and symmetric, the GFT matrix  $\mathbf{F}$  is an orthogonal matrix. Recall from (8) that

$$\mathbf{F}_{\text{I}}^{\mathbf{a}} = \mathbf{V} \mathbf{\Lambda}_F^{\mathbf{a}} \mathbf{V}^{-1}, \quad (19)$$

where  $\mathbf{V}$  is the eigenvector matrix of  $\mathbf{F}$  and satisfies  $\mathbf{V}^{-1} = \mathbf{V}^{\text{H}}$ , and  $\mathbf{\Lambda}_F^{\mathbf{a}} = \text{diag}(\lambda_0^{a_0}, \lambda_1^{a_1}, \dots, \lambda_{N-1}^{a_{N-1}})$  with  $|\lambda_i| = 1$  for all  $i$ .

Thus, we have

$$\begin{aligned} \mathbf{F}_{\text{I}}^{\mathbf{a}} (\mathbf{F}_{\text{I}}^{\mathbf{a}})^{\text{H}} &= \mathbf{V} \mathbf{\Lambda}_F^{\mathbf{a}} \mathbf{V}^{-1} (\mathbf{V} \mathbf{\Lambda}_F^{\mathbf{a}} \mathbf{V}^{-1})^{\text{H}} \\ &= \mathbf{V} \mathbf{\Lambda}_F^{\mathbf{a}} (\mathbf{\Lambda}_F^{\mathbf{a}})^{\text{H}} \mathbf{V}^{-1} \end{aligned} \quad (20)$$

where

$$\mathbf{\Lambda}_F^{\mathbf{a}} (\mathbf{\Lambda}_F^{\mathbf{a}})^{\text{H}} = \text{diag}(|\lambda_0^{a_0}|^2, |\lambda_1^{a_1}|^2, \dots, |\lambda_{N-1}^{a_{N-1}}|^2) = \mathbf{I}_N. \quad (21)$$

Therefore, we arrive the required result.  $\square$

**Remark 2:** Even when the GSO is real and symmetric, the MPGFRFT-II matrix  $\mathbf{F}_{\text{II}}^{\mathbf{a}}$  is generally not unitary, because

$$\begin{aligned} \mathbf{F}_{\text{II}}^{\mathbf{a}} (\mathbf{F}_{\text{II}}^{\mathbf{a}})^{\text{H}} &= \sum_{n=0}^{N-1} \sum_{m=0}^{N-1} C_{n,a_n}^{\text{II}} \overline{C_{m,a_m}^{\text{II}}} \mathbf{F}^n (\mathbf{F}^m)^{\text{H}} \\ &= \sum_{n=0}^{N-1} \sum_{m=0}^{N-1} C_{n,a_n}^{\text{II}} \overline{C_{n,a_n}^{\text{II}}} \mathbf{F}^{n-m}, \end{aligned} \quad (22)$$

which is generally not equal to the identity matrix  $\mathbf{I}_N$ .

## B. Properties

Next, we show some properties of the proposed MPGFRFT-I and MPGFRFT-II.

**Property 1 (Identity matrix):** If the order vector  $\mathbf{a} = (0, 0, \dots, 0)$ , the MPGFRFT-I matrix and MPGFRFT-II matrix can both reduce to an identity matrix, that is

$$\mathbf{F}_{\text{I}}^{\mathbf{a}} = \mathbf{F}_{\text{II}}^{\mathbf{a}} = \mathbf{I}_N. \quad (23)$$

**Property 2 (Reduction to GFRFT):** When the order vector  $\mathbf{a} = (a, a, \dots, a)$ , the MPGFRFT-I and MPGFRFT-II both reduce to the GFRFT.

**Property 3 (Reduction to GFT):** When the order vector  $\mathbf{a} = (1, 1, \dots, 1)$ , the MPGFRFT-I and MPGFRFT-II both reduce to the GFT.

**Proof:** The proofs of properties 1–3 are straightforward and thus omitted.  $\square$

**Property 4 (Index additivity):** Let  $\mathbf{a}$  and  $\mathbf{b}$  be two order vectors. For the MPGFRFT-I matrix, the index additivity property holds

$$\mathbf{F}_{\text{I}}^{\mathbf{a}} \mathbf{F}_{\text{I}}^{\mathbf{b}} = \mathbf{F}_{\text{I}}^{\mathbf{a}+\mathbf{b}}. \quad (24)$$

In contrast, the MPGFRFT-II matrix does not satisfy the property.

**Proof:** For the MPGFRFT-I matrix, we have

$$\begin{aligned} \mathbf{F}_{\text{I}}^{\mathbf{a}} \mathbf{F}_{\text{I}}^{\mathbf{b}} &= \mathbf{V} \mathbf{\Lambda}_F^{\mathbf{a}} \mathbf{V}^{-1} \mathbf{V} \mathbf{\Lambda}_F^{\mathbf{b}} \mathbf{V}^{-1} \\ &= \mathbf{V} \mathbf{\Lambda}_F^{\mathbf{a}+\mathbf{b}} \mathbf{V}^{-1} = \mathbf{F}_{\text{I}}^{\mathbf{a}+\mathbf{b}}. \end{aligned} \quad (25)$$

For the MPGFRFT-II matrix, we have

$$\mathbf{F}_{\text{II}}^{\mathbf{a}} \mathbf{F}_{\text{II}}^{\mathbf{b}} = \sum_{n=0}^{N-1} \sum_{m=0}^{N-1} C_{n,a_n}^{\text{II}} C_{m,b_m}^{\text{II}} \mathbf{F}^n \mathbf{F}^m, \quad (26)$$

which, in general, does not reduce to

$$\mathbf{F}_{\text{II}}^{\mathbf{a}+\mathbf{b}} = \sum_{n=0}^{N-1} C_{n,a_n+b_n}^{\text{II}} \mathbf{F}^n. \quad (27)$$

Thus, we arrive the required results.  $\square$

**Property 5 (Reversibility):** The MPGFRFT-I matrix is invertible for any order vector  $\mathbf{a}$ , and its inverse is given by

$$(\mathbf{F}_{\text{I}}^{\mathbf{a}})^{-1} = \mathbf{F}_{\text{I}}^{-\mathbf{a}}. \quad (28)$$

The MPGFRFT-II matrix is invertible if the following condition holds

$$\sum_{n=0}^{N-1} \left( \sum_{k=0}^{N-1} p_{n+1,k+1} \lambda_k^{a_n} \right) \lambda_j^{a_n} \neq 0 \quad (29)$$

for each  $\lambda_j$  ( $j = 0, 1, \dots, N-1$ ).

**Proof:** According to the index additivity of MPGFRFT-I matrix, we have

$$\mathbf{F}_{\text{I}}^{\mathbf{a}} \mathbf{F}_{\text{I}}^{-\mathbf{a}} = \mathbf{F}_{\text{I}}^{\mathbf{0}} = \mathbf{I}_N. \quad (30)$$

Thus, we arrive the required result (28).



Inserting (3) into (16), we have

$$\begin{aligned}\mathbf{F}_{\text{II}}^a &= \sum_{n=0}^{N-1} C_{n,a_n}^{\text{II}} \mathbf{V} (\mathbf{\Lambda}_F)^n \mathbf{V}^{-1} \\ &= \mathbf{V} \left( \sum_{n=0}^{N-1} C_{n,a_n}^{\text{II}} (\mathbf{\Lambda}_F)^n \right) \mathbf{V}^{-1}.\end{aligned}\quad (31)$$

Therefore,  $\mathbf{F}_{\text{II}}^a$  is invertible if and only if the matrix  $\sum_{n=0}^{N-1} C_{n,a_n}^{\text{II}} (\mathbf{\Lambda}_F)^n$  is invertible, which is equivalent to requiring that all diagonal entries of the matrix are nonzero. Thus, we arrive the required result (29).  $\square$

*Property 6 (Index commutativity):* Both MPGFRFT-I and MPGFRFT-II satisfy the index commutativity property, i.e.

$$\mathbf{F}_{\text{I/II}}^a \mathbf{F}_{\text{I/II}}^b = \mathbf{F}_{\text{I/II}}^b \mathbf{F}_{\text{I/II}}^a. \quad (32)$$

*Proof:* For the MPGFRFT-I matrix, we have

$$\mathbf{F}_{\text{I}}^a \mathbf{F}_{\text{I}}^b = \mathbf{F}_{\text{I}}^{a+b} = \mathbf{F}_{\text{I}}^{b+a} = \mathbf{F}_{\text{I}}^b \mathbf{F}_{\text{I}}^a. \quad (33)$$

For MPGFRFT-II, we have

$$\mathbf{F}_{\text{II}}^a \mathbf{F}_{\text{II}}^b = \left( \sum_{n=0}^{N-1} C_{n,a_n}^{\text{II}} \mathbf{F}^n \right) \left( \sum_{m=0}^{N-1} C_{m,b_m}^{\text{II}} \mathbf{F}^m \right) = \mathbf{F}_{\text{I}}^b \mathbf{F}_{\text{I}}^a. \quad (34)$$

Thus, we arrive the required results.  $\square$

*Property 7 (Eigenvalues and eigenvectors):* Assume  $\mathbf{V}$  is unitary. Then, the eigenvectors  $\mathbf{v}_k$  of the GFT matrix  $\mathbf{F}$  are also eigenvectors of the MPGFRFT-I matrix, with corresponding eigenvalues  $\lambda_k^{a_k}$ .

Similarly, the eigenvectors  $\mathbf{v}_k$  of  $\mathbf{F}$  remain the eigenvectors of the MPGFRFT-II matrix, with corresponding eigenvalues given by  $\sum_{n=0}^{N-1} C_{n,a_n}^{\text{II}} \lambda_k^n$ .

*Proof:* If  $\mathbf{V}$  is unitary, we have

$$\mathbf{F}_{\text{I}}^a \mathbf{v}_k = \left( \sum_{m=0}^{N-1} \lambda_m^{a_m} \mathbf{v}_m \mathbf{v}_m^H \right) \mathbf{v}_k = \lambda_k^{a_k} \mathbf{v}_k, \quad (35)$$

and

$$\mathbf{F}_{\text{II}}^a \mathbf{v}_k = \left( \sum_{n=0}^{N-1} C_{n,a_n}^{\text{II}} \mathbf{F}^n \right) \mathbf{v}_k = \sum_{n=0}^{N-1} C_{n,a_n}^{\text{II}} \lambda_k^n \mathbf{v}_k. \quad (36)$$

Thus, we arrive the required results.  $\square$

*Property 8 (Linearity):* Both MPGFRFT-I and MPGFRFT-II are linear transformations:

$$\mathbf{F}_{\text{I/II}}^a (c_1 \mathbf{x} + c_2 \mathbf{y}) = c_1 \mathbf{F}_{\text{I/II}}^a \mathbf{x} + c_2 \mathbf{F}_{\text{I/II}}^a \mathbf{y}. \quad (37)$$

*Proof:* For MPGFRFT-I, we have

$$\begin{aligned}\mathbf{F}_{\text{I}}^a (c_1 \mathbf{x} + c_2 \mathbf{y}) &= c_1 \mathbf{V} \mathbf{\Lambda}_F^a \mathbf{V}^T \mathbf{x} + c_2 \mathbf{V} \mathbf{\Lambda}_F^a \mathbf{V}^T \mathbf{y} \\ &= c_1 \mathbf{F}_{\text{I}}^a \mathbf{x} + c_2 \mathbf{F}_{\text{I}}^a \mathbf{y}.\end{aligned}\quad (38)$$

Similarly, for MPGFRFT-II, we have

$$\begin{aligned}\mathbf{F}_{\text{II}}^a (c_1 \mathbf{x} + c_2 \mathbf{y}) &= c_1 \sum_{n=0}^{N-1} C_{n,a_n}^{\text{II}} \mathbf{F}^n \mathbf{x} + c_2 \sum_{n=0}^{N-1} C_{n,a_n}^{\text{II}} \mathbf{F}^n \mathbf{y} \\ &= c_1 \mathbf{F}_{\text{II}}^a \mathbf{x} + c_2 \mathbf{F}_{\text{II}}^a \mathbf{y}.\end{aligned}\quad (39)$$

Thus, we arrive the required results.  $\square$

### C. Bandlimitedness

In GSP, bandlimitedness plays a fundamental role in sampling, recovery, and filtering [44]–[46]. Extending the concept of bandlimitedness to the MPGFRFT framework, we can define the MPGFRFT bandlimited signals.

*Definition 3:* Let  $\mathbf{x}$  be a graph signal defined over a graph with  $N$  nodes. The signal  $\mathbf{x}$  is said to be  $\mathbf{a}$ -bandlimited in the MPGFRFT-I/II domain if  $\hat{\mathbf{x}}_{\mathbf{a}}^{\text{I/II}}$  is  $K$ -sparse, i.e.,

$$\|\hat{\mathbf{x}}_{\mathbf{a}}^{\text{I/II}}\|_0 = K, \quad K < N. \quad (40)$$

Without loss of generality, we may assume that the last  $N - K$  entries of  $\hat{\mathbf{x}}_{\mathbf{a}}^{\text{I}}$  are zero.

### D. Learnable Order Vector Approach

The MPGFRFT-I and MPGFRFT-II matrices are both constructed as polynomial functions of the fractional order vector  $\mathbf{a} = [a_0, a_1, \dots, a_{N-1}] \in \mathbb{R}^N$ , as defined in (9) and (16). Thus, these transformations are differentiable with respect to  $\mathbf{a}$ . This property enables their integration into deep learning architectures as trainable layers with learnable fractional orders. Motivated by this observation, we treat  $\mathbf{a}$  as a set of trainable parameters rather than fixed constants, and study the analytical form of the gradients required for backpropagation.

*Theorem 3:* The gradient of the MPGFRFT matrix  $\mathbf{F}_{\text{I/II}}^a$  with respect to the order vector  $\mathbf{a} = [a_0, a_1, \dots, a_{N-1}] \in \mathbb{R}^N$  is a third-order tensor defined as

$$\dot{\mathbf{F}}_{\text{I/II}}^a = \frac{\partial (\mathbf{F}_{\text{I/II}}^a)}{\partial \mathbf{a}} = \left[ \frac{\partial \mathbf{F}_{\text{I/II}}^a}{\partial a_0}, \frac{\partial \mathbf{F}_{\text{I/II}}^a}{\partial a_1}, \dots, \frac{\partial \mathbf{F}_{\text{I/II}}^a}{\partial a_{N-1}} \right], \quad (41)$$

where the  $k$ -th slice of the tensor corresponds to the partial derivative with respect to  $a_k$ . Specifically, we have

$$\frac{\partial \mathbf{F}_{\text{I}}^a}{\partial a_k} = \sum_{n=0}^{N-1} (p_{n+1,k+1} \lambda_k^{a_k} \ln \lambda_k) \mathbf{F}^n, \quad (42)$$

for the MPGFRFT-I case, and

$$\frac{\partial \mathbf{F}_{\text{II}}^a}{\partial a_k} = \left( \sum_{j=0}^{N-1} p_{k+1,j+1} \lambda_j^{a_k} \ln \lambda_j \right) \mathbf{F}^k, \quad (43)$$

for the MPGFRFT-II case.

*Proof:* It is obvious that

$$\frac{\partial (\mathbf{F}_{\text{I/II}}^a)}{\partial a_k} = \sum_{n=0}^{N-1} \frac{\partial C_{n,a_n}^{\text{I/II}}}{\partial a_k} \mathbf{F}^n \quad (44)$$

Differentiating the MPGFRFT-I coefficient  $C_{n,a_n}^{\text{I}}$  with respect to  $a_k$  gives

$$\frac{\partial C_{n,a_n}^{\text{I}}}{\partial a_k} = p_{n+1,k+1} \lambda_k^{a_k} \ln \lambda_k. \quad (45)$$

Differentiating the MPGFRFT-II coefficient  $C_{n,a_n}^{\text{II}}$  with respect to  $a_k$  gives

$$\frac{\partial C_{n,a_n}^{\text{II}}}{\partial a_k} = \begin{cases} \sum_{j=0}^{N-1} p_{k+1,j+1} \lambda_j^{a_k} \ln \lambda_j & k = n \\ 0 & k \neq n \end{cases} \quad (46)$$

Therefore, we arrive the required results.  $\square$

We construct a differentiable MPGRFT layer, where the forward pass at  $l$ -th layer is

$$\mathbf{x}^{(l)} = \varphi \left( \mathbf{F}_{I/\Pi}^a \mathbf{x}^{(l-1)} \right) \quad (47)$$

with  $\varphi$  denoting any differentiable activation function. The learning process involves minimizing a task-specific loss function  $\mathcal{L}$ , with gradients of the form

$$\frac{\partial \mathcal{L}}{\partial \mathbf{a}} = (\nabla_{\mathbf{x}^{(l)}} \mathcal{L})^\top \frac{\partial \mathbf{x}^{(l)}}{\partial \mathbf{a}} \quad (48)$$

with

$$\frac{\partial \mathbf{x}^{(l)}}{\partial \mathbf{a}} = \dot{\varphi} \left( \mathbf{F}_{I/\Pi}^a \mathbf{x}^{(l-1)} \right) \odot \left( \dot{\mathbf{F}}_{I/\Pi}^a \mathbf{x}^{(l-1)} \right), \quad (49)$$

where  $\odot$  denotes element-wise multiplication and  $\dot{\mathbf{F}}_{I/\Pi}^a$  is given by Theorem 3. The order vector is then updated via standard stochastic gradient descent

$$\mathbf{a}^{(t+1)} = \mathbf{a}^{(t)} - \gamma \nabla_{\mathbf{a}} \mathcal{L}, \quad (50)$$

where  $\gamma$  is the learning rate.

While our approach is rooted in the multiple-parameter setting of MPGRFT, it also generalizes prior scalar-order learning schemes. Recent work on the GFRFT proposed learning a scalar fractional order  $a$  to improve transform adaptability [33]. This scalar-order approach imposes a uniform spectral transformation and may not be sufficient for graph signals with complex spectral diversity. In contrast, our learnable order vector approach allows each spectral component to evolve independently, enabling stronger task-specific adaptation. Notably, when the order vector is constrained such that  $a_0 = a_1 = \dots = a_{N-1}$ , our method naturally reduces to the scalar-order GFRFT as a special case.

#### IV. SPECTRAL COMPRESSION UNDER ULTRA-LOW COMPRESSION RATIOS

Traditional transform-based compression methods, such as those using wavelet transform, GFT, or GFRFT [36] rely on projecting signals onto pre-defined orthonormal systems and retaining the largest transform coefficients. However, under ultra-low compression ratios where only a handful of coefficients can be preserved, fixed bases often fail to retain essential structure, especially when the signal does not align well with the chosen basis. To tackle this issue, in this section, we propose a data-driven spectral compression method that constructs a custom unitary transform matrix by treating the signal itself as a basis vector, thereby maximizing alignment between the signal and its transform domain. This approach is particularly effective when only 1 or very few coefficients can be retained, enabling meaningful compression even in such harsh constraints.

To evaluate the performance of the compression, we employ the following three metrics [36].

The relative error (RE) is defined as

$$\text{RE} = \frac{\|\mathbf{x} - \mathbf{x}_{\text{com}}\|_1}{\|\mathbf{x}\|_1}. \quad (51)$$

The normalized root mean square (NRMS) is defined as

$$\text{NRMS} = \frac{\|\mathbf{x} - \mathbf{x}_{\text{com}}\|_2}{\|\mathbf{x} - \mu_{\text{ori}} \mathbf{1}_N\|_1}, \quad (52)$$

where  $\mu_{\text{ori}}$  is the mean of the original signal  $\mathbf{x}$ .

The correlation coefficient (CC) is defined as

$$\text{CC} = \frac{\|(\mathbf{x} - \mu_{\text{ori}} \mathbf{1}_N) \odot (\mathbf{x}_{\text{com}} - \mu_{\text{com}} \mathbf{1}_N)\|_1}{\|\mathbf{x} - \mu_{\text{ori}} \mathbf{1}_N\|_2 \|\mathbf{x}_{\text{com}} - \mu_{\text{com}} \mathbf{1}_N\|_2}, \quad (53)$$

where  $\mu_{\text{com}}$  is the mean of the compressed signal  $\mathbf{x}_{\text{com}}$ .

Let  $\mathbf{x} \in \mathbb{R}^N$  be a signal to be compressed. Instead of projecting  $\mathbf{x}$  onto a fixed basis, such as GFT basis, GFRFT basis, and MPGRFT basis, we construct the MPGRFT matrix according to the signal  $\mathbf{x}$ . we assume that  $\mathbf{x}$  is the first column of the Hermitian transpose of a unitary matrix, i.e.,

$$\mathbf{x} = (\mathbf{F}^a)^H \mathbf{e}_1, \quad (54)$$

where  $\mathbf{e}_1 = (1, 0, \dots, 0)^\top$ , and  $\mathbf{F}^a \in \mathbb{C}^{N \times N}$  is a MPGRFT matrix parameterized by an order vector  $\mathbf{a}$ . Our goal is to reconstruct this matrix solely based on  $\mathbf{x}$ . The core idea is to treat the normalized signal as the first column of a Hermitian matrix and complete the basis using Gram-Schmidt orthogonalization. The resulting unitary matrix can then be inverted to define a custom spectral domain. The complete procedure is presented as pseudocode in Algorithm 1.

---

#### Algorithm 1 Spectral Compression under Ultra-Low Compression Ratios

---

**Require:** Signal  $\mathbf{x} \in \mathbb{R}^N$ , compression ratio  $r \in (0, 1)$

**Ensure:** Compressed signal  $\mathbf{x}_{\text{com}}$ , transform matrix  $\mathbf{F}^a$ , RE, NRMS, CC

---

- 1: **Step 1: Construct unitary basis from the signal**
  - 2: Normalize  $\mathbf{q}_1 = \mathbf{x} / \|\mathbf{x}\|$
  - 3: Initialize  $\mathbf{Q} = [\mathbf{q}_1]$
  - 4: **for**  $i = 2$  to  $N$  **do**
  - 5:   Generate random vector  $\mathbf{r}_i \in \mathbb{C}^N$
  - 6:   Orthogonalize:  $\mathbf{r}'_i = \mathbf{r}_i - \sum_{j=1}^{i-1} \langle \mathbf{r}_i, \mathbf{q}_j \rangle \mathbf{q}_j$
  - 7:   Normalize:  $\mathbf{q}_i = \mathbf{r}'_i / \|\mathbf{r}'_i\|$
  - 8:   Append  $\mathbf{q}_i$  to  $\mathbf{Q}$
  - 9: **end for**
  - 10: Define  $(\mathbf{F}^a)^H = \mathbf{Q}$
  - 11: Compute  $\mathbf{F}^a = (\mathbf{Q})^{-H}$
  - 12: **Step 2: Apply MPGRFT**
  - 13: Transform:  $\hat{\mathbf{x}}_a = \mathbf{F}^a \mathbf{x}$
  - 14: **Step 3: Coefficient selection and compression**
  - 15: Compute index set  $\mathcal{I}$  of the top  $[rN]$  largest coefficients in magnitude
  - 16: Set  $\hat{\mathbf{x}}_a[i] = 0$  for all  $i \notin \mathcal{I}$
  - 17: **Step 4: Inverse transform for reconstruction**
  - 18: Reconstruct:  $\mathbf{x}_{\text{com}} = (\mathbf{F}^a)^{-1} \hat{\mathbf{x}}_a$
  - 19: Compute RE, NRMS and CC
- 

The proposed method offers near-ideal compression by preserving signal integrity with just a single retained coefficient, making it well-suited for resource-limited transmission or noisy environments. Its inherently unitary basis ensures perfect invertibility and numerical stability.

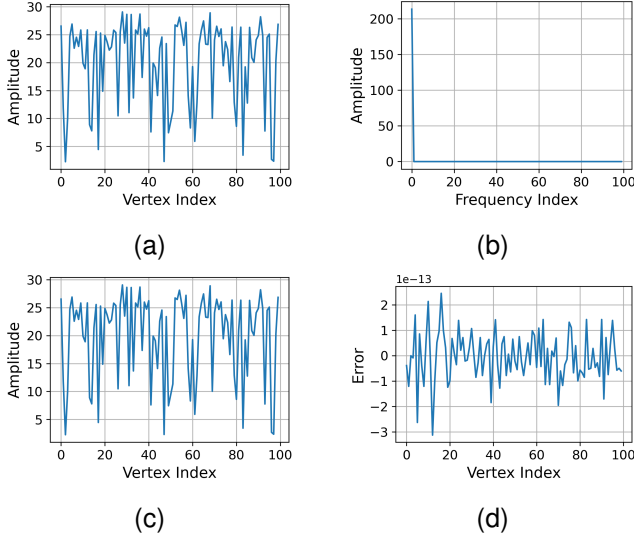


Fig. 2. Compression results of SST under  $r = 0.01$ : (a) Original signal; (b) Spectral signal; (c) Compressed signal; (d) Compression error.

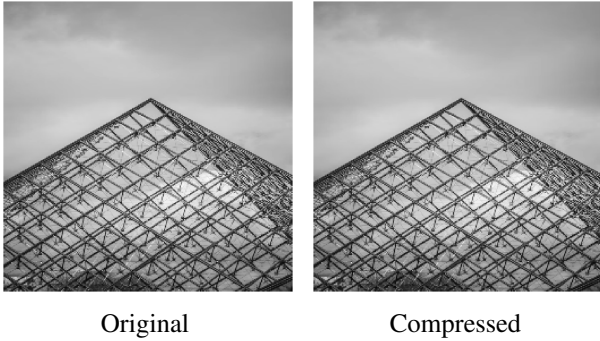


Fig. 3. Compression results of rooftop image under  $r = 0.005$ .

To evaluate the performance of the proposed method under ultra-low compression ratios, we apply it to the sea surface temperature (SST) dataset [47], using the first column and setting the compression ratio to  $r = 0.01$ . As shown in Fig. 2, the original and reconstructed signals are nearly indistinguishable, indicating that the essential information is well preserved. The spectral representation shows a highly concentrated energy distribution, which enables effective compression. Moreover, the residual error remains at the order of  $10^{-13}$ . Quantitatively, the reconstruction yields a RE of  $5.99 \times 10^{-15}$ , a NRMS of  $1.74 \times 10^{-14}$ , and a CC of 1.0000, indicating almost lossless reconstruction.

In addition, we evaluate the method on a  $256 \times 256$  rooftop image, which is divided into 256 non-overlapping blocks of size  $16 \times 16$ , each compressed with a ratio of  $r = 0.005$ . As illustrated in Fig. 3, the reconstructed image maintains high visual quality with no perceptible difference from the original. The achieved RE/NRMS/CC metrics are  $0.00 \times 10^0 / 0.00 \times 10^0 / 0.9999$ , further demonstrating the effectiveness of MPGFRFT in structured signal compression tasks.

## V. APPLICATIONS

In this section, we evaluate the proposed MPGFRFT framework through a series of experiments. We verify key theoretical properties of the framework, including its multi-layer transform learning capability and the effectiveness of order vector learning. These experiments provide empirical support for the design principles of MPGFRFT. We demonstrate the practical benefits of the method in several tasks, including compression, denoising, and image encryption and decryption.

The experiments are performed on both synthetic and real-world datasets. The real-world datasets include the SST, particulate matter 2.5 (PM-25), and COVID-19 global (COVID) datasets, as introduced in [47]. In addition, we evaluate the performance on several image datasets, including depth images from Teddy [48] and Art [49], natural images from [50], the rooftop image used in Section IV, and an airplane image (F-16) from [51].

### A. Transform Learning

Motivated by the index additivity property of MPGFRFT-I, we design a learnable  $l$ -layer MPGFRFT-I network, where each layer is parameterized by a transform order vector  $\mathbf{a}_l \in \mathbb{R}^N$ . For any input signal  $\mathbf{x} \in \mathbb{R}^N$ , the whole network can be defined as

$$\hat{\mathbf{y}} = \left( \prod_{l=1}^L \mathbf{F}_I^{\mathbf{a}_l} \right) \mathbf{x} = \mathbf{F}_I^{\sum_{l=1}^L \mathbf{a}_l} \mathbf{x}, \quad (55)$$

where  $\hat{\mathbf{y}}$  is the estimation of the MPGFRFT-I network. To train the network, we define the supervision target as  $\mathbf{y} = \mathbf{F}_I^{\mathbf{a}_{\text{ori}}} \mathbf{x}$ , where  $\mathbf{a}_{\text{ori}} \in \mathbb{R}^N$  is the original transform order vector. The estimated output  $\hat{\mathbf{y}}$  is optimized to match the target using the mean squared error (MSE) loss

$$\mathcal{L}_{\text{MSE}} = \frac{1}{N} \|\hat{\mathbf{y}} - \mathbf{y}\|_2^2. \quad (56)$$

In contrast, MPGFRFT-II does not satisfy the additivity property and is therefore unsuitable for layer-wise composition. As a result, we focus our experiments solely on MPGFRFT-I. We evaluate the network on a randomly generated weighted directed graph with  $N = 90$  vertices and adjacency matrix  $\mathbf{A} \in \mathbb{R}^{90 \times 90}$ . The input graph signal  $\mathbf{x} \in \mathbb{R}^{90}$  is generated randomly. The transform order vector  $\mathbf{a}_{\text{ori}}$  is initialized with a block structure: the first 30 nodes use order 0.7, the middle 30 use 0.2, and the last 30 use 0.5. This can be written as

$$\mathbf{a}_{\text{ori}} = \underbrace{(0.7, \dots, 0.7)}_{30}, \underbrace{(0.2, \dots, 0.2)}_{30}, \underbrace{(0.5, \dots, 0.5)}_{30}, \quad (57)$$

which we refer to as the three-block setting and abbreviate as  $\mathbf{a}_{\text{ori}} = (0.7, 0.2, 0.5)_{30}$ . We also consider a five-block setting with  $\mathbf{a}_{\text{ori}} = (0.3, 0.4, 0.5, 0.6, 0.7)_{18} \in \mathbb{R}^{90}$ . For each setting, we consider  $L \in \{1, 2, 3\}$  layers in the network. The transform orders are initialized using  $\mathbf{a}_{\text{ori}}$  with a learning rate of 0.001. We train the network using the Adam optimizer for 2000 epochs under the  $(0.7, 0.2, 0.5)_{30}$  setting, and for 3000 epochs under the  $(0.3, 0.4, 0.5, 0.6, 0.7)_{18}$  setting. Note that the output at epoch 1 corresponds exactly to the original

TABLE I  
CONVERGENCE OF THE TRANSFORM ORDERS IN TRANSFORM LEARNING EXPERIMENT FOR LEARNABLE MPGRFT-I.

$\mathbf{a}_{\text{ori}} = (0.7000, 0.2000, 0.5000)_{30}$						
$L = 1$			$L = 2$			
Epoch	$\mathbf{a}_1$	loss	$\mathbf{a}_1$	$\mathbf{a}_2$	sum	loss
1	(0.0000, 0.1000, 0.2000)	1.45	(0.0000, 0.1000, 0.2000)	(0.5000, 0.2000, 0.3000)	(0.5000, 0.3000, 0.5000)	$3.82 \times 10^{-1}$
500	(0.4802, 0.0577, 0.3803)	$2.33 \times 10^{-1}$	(0.1000, 0.5000, 0.2000)	(0.6000, 0.1500, 0.3000)	(0.7000, 0.2000, 0.5000)	$2.44 \times 10^{-10}$
1000	(0.6881, 0.1886, 0.4910)	$9.90 \times 10^{-4}$	(0.1000, 0.5000, 0.2000)	(0.6000, 0.1500, 0.3000)	(0.7000, 0.2000, 0.5000)	$2.14 \times 10^{-10}$
1500	(0.6999, 0.1999, 0.4999)	$3.13 \times 10^{-8}$	(0.1000, 0.5000, 0.2000)	(0.6000, 0.1500, 0.3000)	(0.7000, 0.2000, 0.5000)	$2.22 \times 10^{-10}$
2000	(0.7000, 0.2000, 0.5000)	$2.18 \times 10^{-11}$	(0.1000, 0.5000, 0.2000)	(0.6000, 0.1500, 0.3000)	(0.7000, 0.2000, 0.5000)	$2.01 \times 10^{-10}$
$L = 3$						
Epoch	$\mathbf{a}_1$	$\mathbf{a}_2$	$\mathbf{a}_3$	sum	loss	
1	(0.0000, 0.1000, 0.2000)	(0.5000, 0.2000, 0.3000)	(0.3000, 0.2000, 0.5000)	(0.8000, 0.5000, 1.0000)	$8.84 \times 10^{-1}$	
500	(-0.332, 0.0001, 0.0336)	(0.4667, 0.1001, 0.1336)	(0.2667, 0.1001, 0.3336)	(0.7002, 0.2004, 0.5007)	$1.52 \times 10^{-6}$	
1000	(-0.333, 0.0000, 0.0333)	(0.4667, 0.1000, 0.1333)	(0.2666, 0.1000, 0.3333)	(0.7000, 0.2000, 0.5000)	$4.42 \times 10^{-10}$	
1500	(-0.333, 0.0000, 0.0333)	(0.4667, 0.1000, 0.1333)	(0.2666, 0.1000, 0.3333)	(0.7000, 0.2000, 0.5000)	$4.55 \times 10^{-10}$	
2000	(-0.333, 0.0000, 0.0333)	(0.4667, 0.1000, 0.1333)	(0.2666, 0.1000, 0.3333)	(0.7000, 0.2000, 0.5000)	$4.53 \times 10^{-10}$	
$\mathbf{a}_{\text{ori}} = (0.3000, 0.4000, 0.5000, 0.6000, 0.7000)_{18}$						
$L = 1$			$L = 2$			
Epoch	$\mathbf{a}_1$	loss	$\mathbf{a}_1$	$\mathbf{a}_2$	sum	loss
1	(0.5000, 0.7000, 0.3000, 0.1000, 0.0000)	2.29	(0.5000, 0.7000, 0.3000, 0.1000, 0.0000)	(0.4000, 0.3000, 0.5000, 0.2000, 0.1000)	(0.9000, 1.0000, 0.8000, 0.3000, 0.1000)	4.32
1000	(0.2894, 0.3816, 0.4759, 0.5594, 0.6392)	$7.14 \times 10^{-3}$	(0.2048, 0.4065, 0.1539, 0.2548, 0.3068)	(0.1048, 0.0065, 0.3539, 0.3548, 0.4068)	(0.3096, 0.4131, 0.5077, 0.6095, 0.7136)	$7.87 \times 10^{-4}$
2000	(0.2994, 0.3992, 0.4994, 0.5991, 0.6988)	$4.09 \times 10^{-6}$	(0.2000, 0.4000, 0.1500, 0.2500, 0.3000)	(0.1000, 0.0000, 0.3500, 0.3500, 0.4000)	(0.3000, 0.4000, 0.5000, 0.6000, 0.7000)	$1.91 \times 10^{-9}$
3000	(0.3000, 0.4000, 0.5000, 0.6000, 0.7000)	$2.77 \times 10^{-11}$	(0.2000, 0.4000, 0.1500, 0.2500, 0.3000)	(0.1000, -0.0000, 0.3500, 0.3500, 0.4000)	(0.3000, 0.4000, 0.5000, 0.6000, 0.7000)	$5.50 \times 10^{-11}$
$L = 3$						
Epoch	$\mathbf{a}_1$	$\mathbf{a}_2$	$\mathbf{a}_3$	sum	loss	
1	(0.5000, 0.7000, 0.3000, 0.1000, 0.0000)	(0.4000, 0.3000, 0.5000, 0.2000, 0.1000)	(0.1000, 0.0000, 0.2000, 0.7000, 0.9000)	(1.0000, 1.0000, 1.0000, 1.0000, 1.0000)	3.08	
1000	(0.2671, 0.5003, 0.1335, -0.0332, -0.0998)	(0.1671, 0.1003, 0.3335, 0.0668, 0.0002)	(-0.1329, -0.1997, 0.0335, 0.5668, 0.8002)	(0.3013, 0.4008, 0.5005, 0.6004, 0.7005)	$4.41 \times 10^{-6}$	
2000	(0.2667, 0.5000, 0.1333, -0.0333, -0.1000)	(0.1667, 0.1000, 0.3333, 0.0667, -0.0000)	(-0.1333, -0.2000, 0.0333, 0.5667, 0.8000)	(0.3000, 0.4000, 0.5000, 0.6000, 0.7000)	$3.16 \times 10^{-10}$	
3000	(0.2667, 0.5000, 0.1333, -0.0333, -0.1000)	(0.1667, 0.1000, 0.3333, 0.0667, -0.0000)	(-0.1333, -0.2000, 0.0333, 0.5667, 0.8000)	(0.3000, 0.4000, 0.5000, 0.6000, 0.7000)	$3.37 \times 10^{-10}$	

transform using  $\mathbf{a}_{\text{ori}}$ , i.e., without learning. Table I summarizes the results under each configuration. For simplicity, the order vectors shown in the table omit subscripts. The outputs under different layer configurations confirm the additive property of MPGRFT-I, since applying multiple layers yields results equivalent to a single transform with the summed order vector.

### B. Order Vector Learning

Consider the model  $\mathbf{y} = \mathbf{x} + \mathbf{n}$ , where  $\mathbf{x}$  denotes the clean graph signal,  $\mathbf{n}$  represents the additive noise, and  $\mathbf{y}$  is the noisy observation. We aim to investigate the separability between signal and noise in the transform domains, based on the first 10 normalized columns of the SST dataset [47]. We construct an 8-nearest neighbor (8-NN) graph. Two  $\mathbf{a}_{\text{ori}}$ -bandlimited graph signals are designed with  $\mathbf{a}_{\text{ori}} = (0.35, 0.65)_{50} \in \mathbb{R}^{100}$ : the graph signal  $\mathbf{x}_1$ , which is  $K$ -sparse in the MPGRFT-I domain, and the graph signal  $\mathbf{x}_2$ , which is  $K$ -sparse in the MPGRFT-II domain. The noise  $\mathbf{n}$  is generated to be “high-frequency” in the  $\mathbf{a}_{\text{ori}}$ -domain, with  $0 \leq c_0 \leq K$  overlapping entries with the graph signal, i.e.,

$$\hat{\mathbf{n}}_{\mathbf{a}}^{\text{I/II}} = \left(0, \dots, 0, \hat{n}_{\mathbf{a}, K-c_0}^{\text{I/II}}, \dots, \hat{n}_{\mathbf{a}, N-1}^{\text{I/II}}\right)^{\text{T}}.$$

To recover the graph signal from noisy observations, we apply the spectral-domain filtering strategy

$$\tilde{\mathbf{x}} = \mathbf{F}_T^{-1} \mathbf{H} \mathbf{F}_T \mathbf{y}, \quad (58)$$

where  $\mathbf{F}_T$  denotes the transformation matrix (either GFRFT, MPGRFT-I, or MPGRFT-II), and  $\mathbf{H}$  is the diagonal graph filter. We consider both the ideal low-pass filter  $\mathbf{H}_K = \text{diag}([\mathbf{1}_K^{\text{T}}, \mathbf{0}_{N-K}^{\text{T}}])$ , and the trainable diagonal filter  $\mathbf{H}_{\text{learn}} = \text{diag}(h_1, h_2, \dots, h_N)$ , where each entry  $h_i$  serves as a learnable parameter optimized during training.

The signal recovery experiments are conducted under various noise levels  $\sigma = \{0.2, 0.4, 0.6\}$  and overlap values  $c_0 = \{0, 5, 10\}$ , with the sparsity level set to  $K = 70$ . The parameters of the network are optimized by minimizing the MSE loss over 1000 training epochs, using a learning

rate of 0.005. We refer to GFRFT- $\mathbf{H}_K$  and GFRFT- $\mathbf{H}_{\text{learn}}$  as the methods using GFRFT with a fixed ideal low-pass filter  $\mathbf{H}_K$  and a learnable filter  $\mathbf{H}_{\text{learn}}$ , respectively. To facilitate the presentation of results in MPGRFT-based methods, we constrain the learnable transform order vector to have only two distinct parameters, such that  $\mathbf{a}_{\text{train}} = (a_1, a_2)_{50} \in \mathbb{R}^{100}$ . The signal-to-noise ratio (SNR) is defined as

$$\text{SNR} = 20 \log_{10} \left( \frac{\|\mathbf{x}\|_2}{\|\mathbf{x} - \tilde{\mathbf{x}}\|_2} \right). \quad (59)$$

Tables II and III report the SNR and MSE results for  $\mathbf{a}_{\text{ori}}$ -bandlimited graph signals  $\mathbf{x}_1$  and  $\mathbf{x}_2$ , which are 70-sparse in the MPGRFT-I and MPGRFT-II domains, respectively. We observe that the MPGRFT-based methods are capable of achieving complete separation between signal and noise when there is no overlap  $c_0 = 0$ . In the cases where the signal and noise are overlapping, the methods based on MPGRFT with a learnable filter  $\mathbf{H}_{\text{learn}}$  consistently outperform all other approaches, yielding both higher SNR and lower MSE. In all cases, the learned transform order vectors in the MPGRFT-based filtering methods remain close to the original design  $\mathbf{a}_{\text{ori}}$ , indicating the stability and robustness of the proposed learning framework.

### C. Compression

Data compression is a fundamental task in GSP, enabling efficient storage and transmission by reducing data amount while retaining essential information. In this part, two compression paradigms. First, in 1) *Synthetic-Data Compression* and 2) *Real-Data Compression*, we adopt a straightforward MPGRFT-based scheme, which applies a fixed transform followed by coefficient truncation, as described in Steps 2-4 of Algorithm 1. Then, in 3) *Learnable Compression*, we present a novel approach in which the order vector is treated as trainable parameters. By optimizing the order vector for sparsity, this approach enables adaptive spectral compression that enhances performance under fixed graph structures.

TABLE II

SNR AND MSE RESULTS FOR TRANSFORM ORDER VECTOR LEARNING EXPERIMENT ON THE SST DATASET: CASE OF  $\mathbf{a}_{\text{ori}}$ -BANDLIMITED GRAPH SIGNAL  $\mathbf{x}_1$  IN THE MPGFRFT-I DOMAIN.

Method	SNR MSE (order)	$c_0 = 0$			$c_0 = 5$			$c_0 = 10$		
		$\sigma = 0.2$	$\sigma = 0.4$	$\sigma = 0.6$	$\sigma = 0.2$	$\sigma = 0.4$	$\sigma = 0.6$	$\sigma = 0.2$	$\sigma = 0.4$	$\sigma = 0.6$
		8.7381 $2.79 \times 10^{-2}$	2.7175 $1.12 \times 10^{-1}$	-0.8043 $2.51 \times 10^{-1}$	8.4145 $3.01 \times 10^{-2}$	2.3939 $1.20 \times 10^{-1}$	-1.128 $2.71 \times 10^{-1}$	7.9876 $3.32 \times 10^{-2}$	1.967 $1.33 \times 10^{-1}$	-1.5548 $2.99 \times 10^{-1}$
GFRFT- $\mathbf{H}_K$		15.8931 $5.38 \times 10^{-3}$ (-0.3889)	15.243 $6.24 \times 10^{-3}$ (-0.3882)	14.3384 $7.69 \times 10^{-3}$ (-0.3874)	14.3445 $7.68 \times 10^{-3}$ (-0.3899)	11.3069 $1.55 \times 10^{-2}$ (-0.3915)	8.6627 $2.84 \times 10^{-2}$ (-0.3934)	13.3529 $9.65 \times 10^{-3}$ (-0.3918)	9.5228 $2.33 \times 10^{-2}$ (-0.3985)	6.5698 $4.60 \times 10^{-2}$ (-0.4067)
GFRFT- $\mathbf{H}_{\text{learn}}$		17.6706 $3.57 \times 10^{-3}$ (-0.3842)	16.1784 $5.03 \times 10^{-3}$ (-0.3876)	15.2068 $6.30 \times 10^{-3}$ (-0.3877)	15.7151 $5.60 \times 10^{-3}$ (-0.3883)	12.9802 $1.05 \times 10^{-2}$ (-0.3905)	11.5527 $1.46 \times 10^{-2}$ (-0.3935)	14.5927 $7.25 \times 10^{-3}$ (-0.382)	11.2636 $1.56 \times 10^{-2}$ (-0.3878)	9.1563 $2.54 \times 10^{-2}$ (-0.3942)
MPGFRFT-I- $\mathbf{H}_K$		<b>152.9720</b> <b><math>1.05 \times 10^{-16}</math></b> (0.3500, 0.6500)	<b>152.3098</b> <b><math>1.23 \times 10^{-16}</math></b> (0.3500, 0.6500)	<b>151.3906</b> <b><math>1.52 \times 10^{-16}</math></b> (0.3500, 0.6500)	19.5777 $2.30 \times 10^{-3}$ (0.3497, 0.6524)	13.5591 $9.20 \times 10^{-3}$ (0.3488, 0.6584)	10.0400 $2.07 \times 10^{-2}$ (0.3476, 0.6661)	16.7497 $4.41 \times 10^{-3}$ (0.3523, 0.6509)	10.7343 $1.76 \times 10^{-2}$ (0.3582, 0.6530)	7.219 $3.96 \times 10^{-2}$ (0.3656, 0.6553)
MPGFRFT-I- $\mathbf{H}_{\text{learn}}$		93.9045 $8.50 \times 10^{-11}$ (0.3500, 0.6500)	75.2584 $6.22 \times 10^{-9}$ (0.3500, 0.6500)	63.9131 $8.48 \times 10^{-8}$ (0.3503, 0.6500)	<b>20.4327</b> <b><math>1.89 \times 10^{-3}</math></b> (0.3504, 0.6541)	<b>15.5227</b> <b><math>5.85 \times 10^{-3}</math></b> (0.3524, 0.6484)	<b>13.3521</b> <b><math>9.65 \times 10^{-3}</math></b> (0.3570, 0.6358)	<b>17.9328</b> <b><math>3.36 \times 10^{-3}</math></b> (0.3522, 0.6457)	<b>12.7853</b> <b><math>1.10 \times 10^{-2}</math></b> (0.3549, 0.6412)	<b>10.1705</b> <b><math>2.01 \times 10^{-2}</math></b> (0.3584, 0.6487)

TABLE III

SNR AND MSE RESULTS FOR TRANSFORM ORDER VECTOR LEARNING EXPERIMENT ON THE SST DATASET: CASE OF  $\mathbf{a}_{\text{ori}}$ -BANDLIMITED GRAPH SIGNAL  $\mathbf{x}_2$  IN THE MPGFRFT-II DOMAIN.

Method	SNR MSE (order)	$c_0 = 0$			$c_0 = 5$			$c_0 = 10$		
		$\sigma = 0.2$	$\sigma = 0.4$	$\sigma = 0.6$	$\sigma = 0.2$	$\sigma = 0.4$	$\sigma = 0.6$	$\sigma = 0.2$	$\sigma = 0.4$	$\sigma = 0.6$
		8.3247 $2.85 \times 10^{-2}$	2.3041 $1.14 \times 10^{-1}$	-1.2178 $2.57 \times 10^{-1}$	7.9782 $3.09 \times 10^{-2}$	1.9576 $1.24 \times 10^{-1}$	-1.5643 $2.78 \times 10^{-1}$	7.6496 $3.34 \times 10^{-2}$	1.6290 $1.33 \times 10^{-1}$	-1.8929 $3.00 \times 10^{-1}$
GFRFT- $\mathbf{H}_K$		18.4135 $2.80 \times 10^{-3}$ (-0.3537)	17.82 $3.21 \times 10^{-3}$ (-0.3510)	16.9950 $3.88 \times 10^{-3}$ (-0.3479)	15.7976 $5.11 \times 10^{-3}$ (-0.3540)	11.9272 $1.25 \times 10^{-2}$ (-0.3517)	8.9553 $2.47 \times 10^{-2}$ (-0.3492)	14.3144 $7.19 \times 10^{-3}$ (-0.3566)	9.7074 $2.08 \times 10^{-2}$ (-0.3608)	6.5095 $4.34 \times 10^{-2}$ (-0.3661)
GFRFT- $\mathbf{H}_{\text{learn}}$		19.6593 $2.10 \times 10^{-3}$ (-0.3549)	18.3893 $2.81 \times 10^{-3}$ (-0.3509)	17.4526 $3.49 \times 10^{-3}$ (-0.3481)	16.7256 $4.13 \times 10^{-3}$ (-0.3534)	13.5987 $8.48 \times 10^{-3}$ (-0.3513)	11.9829 $1.23 \times 10^{-2}$ (-0.3533)	15.6327 $5.31 \times 10^{-3}$ (-0.3578)	11.5333 $1.36 \times 10^{-2}$ (-0.3547)	9.0832 $2.40 \times 10^{-2}$ (-0.3555)
MPGFRFT-II- $\mathbf{H}_K$		<b>140.8509</b> <b><math>1.60 \times 10^{-15}</math></b> (0.3500, 0.6500)	<b>140.2130</b> <b><math>1.85 \times 10^{-15}</math></b> (0.3500, 0.6500)	<b>139.3584</b> <b><math>2.25 \times 10^{-15}</math></b> (0.3500, 0.6500)	19.2474 $2.31 \times 10^{-3}$ (0.3498, 0.6503)	13.2272 $9.23 \times 10^{-3}$ (0.3496, 0.6496)	9.7072 $2.08 \times 10^{-2}$ (0.3491, 0.6483)	16.4020 $4.44 \times 10^{-3}$ (0.3518, 0.6486)	10.3858 $1.78 \times 10^{-2}$ (0.3567, 0.6444)	6.8697 $3.99 \times 10^{-2}$ (0.3629, 0.6390)
MPGFRFT-II- $\mathbf{H}_{\text{learn}}$		63.8915 $7.92 \times 10^{-8}$ (0.3501, 0.6501)	67.9671 $3.10 \times 10^{-8}$ (0.3500, 0.6500)	63.5443 $8.58 \times 10^{-8}$ (0.3500, 0.6500)	<b>20.0059</b> <b><math>1.94 \times 10^{-3}</math></b> (0.3505, 0.6508)	<b>15.5035</b> <b><math>5.47 \times 10^{-3}</math></b> (0.3519, 0.6538)	<b>13.5508</b> <b><math>8.57 \times 10^{-3}</math></b> (0.3559, 0.6541)	<b>16.8340</b> <b><math>4.02 \times 10^{-3}</math></b> (0.3568, 0.3118)	<b>12.4974</b> <b><math>1.09 \times 10^{-2}</math></b> (0.3520, 0.6540)	<b>9.7338</b> <b><math>2.06 \times 10^{-2}</math></b> (0.3542, 0.6564)

1) *Synthetic-Data Compression*: We first conduct experiments on synthetic signals. Specifically, we generate signals over the interval  $[-10, 10]$  with  $N = 20$  nodes, and construct two types of graphs: a ring graph and a sensor graph. The compression is performed with ratios  $r \in \{0.3, 0.5, 0.8\}$ . For the MPGFRFT-based compression method, we adopt a four-block structured order vector. Table IV presents the compression results in terms of RE, NRMS, and CC under different compression ratios. The results are obtained using the optimal order vectors searched with a step size of 0.1 for each method. As shown in the table, the MPGFRFT-based methods consistently outperform the GFRFT-based method across all three metrics and all tested compression ratios. Both MPGFRFT-I and MPGFRFT-II achieve lower reconstruction errors and higher correlation, demonstrating its superiority in graph-based data compression.

2) *Real-Data Compression*: To further validate the effectiveness of the proposed compression scheme, we conduct experiments on real-world PM-25 dataset with  $N = 93$ . The signal is constructed by assigning values from different time indices (columns) of the dataset to consecutive node intervals: values from column 34 are assigned to nodes 1–19, column 42 to nodes 20–38, column 36 to nodes 39–57, column 70 to nodes 58–75, and column 66 to nodes 76–93. We use 5-NN graph. The compression is again performed at ratios  $r \in \{0.3, 0.5, 0.8\}$ . For the MPGFRFT-based methods, we use a three-block structured order vector. Table V presents

the compression results on the PM-25 dataset across different compression ratios. As in the synthetic case, the MPGFRFT-based approaches consistently outperform the GFRFT-based method across all evaluation metrics. It achieves notably lower RE and NRMS values and maintains higher CC values, confirming the robustness and adaptability of the multiple-parameter strategy in realistic and spatially heterogeneous graph signal environments.

3) *Learnable Compression*: To achieve optimal data compression in the MPGFRFT domain, we propose a learnable compression strategy that leverages the parametric flexibility of the MPGFRFT matrix. Specifically, we aim to learn the optimal order vector  $\mathbf{a}$  such that the transformed signal  $\hat{\mathbf{x}}_{\mathbf{a}}^{I/II}$  becomes maximally sparse. The objective function is defined as the negative squared  $\ell_2$  norm of the top  $[rN]$  largest coefficients of the transformed signal

$$\mathcal{L} = -\left\| \mathcal{T}_r \left( \hat{\mathbf{x}}_{\mathbf{a}}^{I/II} \right) \right\|_2^2, \quad (60)$$

where  $\mathcal{T}_r(\cdot)$  denotes the truncation operator that retains only the top  $[rN]$  coefficients after sorting in descending order of magnitude, and  $\lfloor \cdot \rfloor$  denotes the floor operation. This formulation encourages the energy of the signal to be concentrated in a small number of transform coefficients, resulting in an effective compression scheme. We optimize  $\mathbf{a}$  via gradient descent using the framework introduced in Section III-D. Algorithm 2 gives the pseudo code for learnable compression using MPGFRFT.

TABLE IV  
COMPRESSION PERFORMANCE ON SYNTHETIC GRAPH SIGNALS.

Ring graph			
RE	$r = 0.3$	$r = 0.5$	$r = 0.8$
GFRFT	47.98% (0.4)	25.78% (1.0)	7.85% (0.1)
MPGFRFT-I	<b>30.37%</b> (1.0, 0.2, 0.3, 0.5)	<b>13.81%</b> (1.0, 0.1, 0.2, 0.5)	<b>1.10%</b> (1.0, 0.1, 0.3, 0.7)
MPGFRFT-II	39.58% (0.9, 1.0, 0.3, 1.0)	24.97% (1.0, 1.0, 0.9, 1.0)	5.77% (1.0, 0.4, 1.0, 0.9)
NRMS	$r = 0.3$	$r = 0.5$	$r = 0.8$
GFRFT	60.77% (0.4)	35.03% (0.4)	11.37% (0.4)
MPGFRFT-I	<b>40.60%</b> (1.0, 0.1, 0.1, 0.1)	<b>17.52%</b> (1.0, 0.1, 0.4, 0.5)	<b>1.25%</b> (1.0, 0.1, 0.3, 0.7)
MPGFRFT-II	58.47% (0.5, 0.6, 0.5, 1.0)	30.43% (1.0, 1.0, 0.5, 1.0)	6.39% (1.0, 0.4, 1.0, 0.9)
CC	$r = 0.3$	$r = 0.5$	$r = 0.8$
GFRFT	93.20% (0.4)	96.40% (0.4)	99.69% (0.4)
MPGFRFT-I	<b>95.64%</b> (0.4, 0.4, 0.9, 0.1)	<b>99.12%</b> (1.0, 0.1, 0.7, 0.6)	<b>99.99%</b> (1.0, 0.1, 0.3, 0.7)
MPGFRFT-II	95.17% (0.4, 1.0, 0.5, 0.1)	98.43% (0.5, 0.1, 0.4, 1.0)	99.94% (0.4, 0.8, 0.5, 0.1)
Sensor graph			
RE	$r = 0.3$	$r = 0.5$	$r = 0.8$
GFRFT	42.07% (0.7)	21.14% (1.0)	3.54% (0.4)
MPGFRFT-I	33.30% (0.1, 0.1, 0.9, 0.3)	15.42% (0.2, 0.6, 1.0, 0.3)	<b>0.83%</b> (0.7, 1.0, 1.0, 0.5)
MPGFRFT-II	<b>24.29%</b> (0.7, 0.1, 0.9, 0.6)	<b>9.96%</b> (0.7, 0.8, 0.1, 0.6)	1.14% (0.9, 0.8, 0.4, 0.5)
NRMS	$r = 0.3$	$r = 0.5$	$r = 0.8$
GFRFT	51.25% (0.9)	26.99% (1.0)	4.65% (0.4)
MPGFRFT-I	38.42% (0.1, 0.1, 0.9, 0.3)	19.64% (0.1, 0.8, 0.5, 1.0)	<b>0.97%</b> (0.7, 1.0, 1.0, 0.5)
MPGFRFT-II	<b>29.19%</b> (0.7, 0.1, 0.9, 0.6)	<b>13.63%</b> (0.7, 0.8, 0.9, 0.6)	1.35% (0.9, 0.8, 0.5, 0.5)
CC	$r = 0.3$	$r = 0.5$	$r = 0.8$
GFRFT	92.89% (0.8)	98.06% (1.0)	99.90% (0.4)
MPGFRFT-I	96.50% (0.9, 0.1, 1.0, 0.1)	98.46% (0.1, 0.4, 0.9, 0.1)	<b>99.99%</b> (0.7, 1.0, 1.0, 0.5)
MPGFRFT-II	<b>96.54%</b> (0.7, 0.9, 0.1, 0.3)	<b>99.16%</b> (0.7, 0.8, 0.1, 0.6)	99.99% (0.9, 0.8, 0.5, 0.5)

According to Theorem 2, when the underlying graph is constructed symmetrically, such as the symmetric  $k$ -NN graphs, the MPGFRFT-I matrix is guaranteed to be unitary. This unitarity implies energy preservation

$$\|\hat{\mathbf{x}}_a\|_2^2 = \|\mathbf{F}_a^T \mathbf{x}\|_2^2 = \|\mathbf{x}\|_2^2. \quad (61)$$

Therefore, maximizing the energy in the top  $[rN]$  spectral coefficients directly implies minimizing the energy in the remaining  $N - [rN]$  coefficients. This property leads to sparse spectral representations, making MPGFRFT-I a powerful tool for compression. However, this property generally does not hold for the MPGFRFT-II matrix, which is non-unitary. In such cases, the transformed energy is not preserved, and the optimization objective does not directly correspond to sparsity

TABLE V  
COMPRESSION PERFORMANCE ON PM-25 DATASET.

RE	$r = 0.3$	$r = 0.5$	$r = 0.8$
GFRFT	39.19% (0.8)	19.89% (0.6)	3.54% (0.1)
MPGFRFT-I	<b>35.04%</b> (1.2, 0.5, 1.1)	19.62% (1.3, 0.9, 0.9)	<b>3.31%</b> (0.9, 0.8, 0.9)
MPGFRFT-II	37.45% (1.2, 1.8, 1.2)	<b>19.44%</b> (1.2, 1.8, 1.2)	3.42% (1.2, 1.8, 1.2)
NRMS	$r = 0.3$	$r = 0.5$	$r = 0.8$
GFRFT	52.67% (1.1)	28.34% (0.6)	6.92% (0.9)
MPGFRFT-I	51.82% (0.7, 0.6, 0.8)	27.63% (1.2, 0.9, 1.1)	<b>4.55%</b> (0.9, 0.8, 0.9)
MPGFRFT-II	<b>50.94%</b> (1.2, 1.8, 1.2)	<b>27.34%</b> (1.2, 1.8, 1.2)	6.21% (1.2, 1.8, 1.2)
CC	$r = 0.3$	$r = 0.5$	$r = 0.8$
GFRFT	92.80% (0.1)	96.59% (0.1)	99.78% (0.9)
MPGFRFT-I	93.01% (0.2, 0.1, 0.1)	<b>97.22%</b> (1.8, 0.9, 0.9)	<b>99.90%</b> (1.5, 1.4, 1.7)
MPGFRFT-II	<b>93.74%</b> (0.2, 0.8, 0.8)	96.97% (1.2, 1.8, 1.2)	99.81% (1.2, 1.8, 1.2)

#### Algorithm 2 Learnable Compression using MPGFRFT

**Require:** Signal  $\mathbf{x} \in \mathbb{R}^N$ , compression ratio  $r$ , learning rate  $\gamma$ , training epochs

**Ensure:** Optimized order vector  $\mathbf{a}_{\text{opt}}$ , RE, NRMS and CC

- 1: Initialize order vector  $\mathbf{a}_{\text{initial}} = (0.5)_N \in \mathbb{R}^N$
- 2: **for**  $t = 1$  to training epochs **do**
- 3:   **Step 1: Operator construction**
- 4:   Construct MPGFRFT matrix:  $(\mathbf{F}_a)^{(t)}$
- 5:   **Step 2: Forward propagation**
- 6:   Transform signal:  $\hat{\mathbf{x}}_a^{(t)} = (\mathbf{F}_a)^{(t)} \mathbf{x}$
- 7:   Truncate:  $\mathbf{z}^{(t)} = \mathcal{T}_r(\hat{\mathbf{x}}_a^{(t)})$
- 8:   **Step 3: Loss calculation and back propagation**
- 9:   Compute loss:  $\mathcal{L}^{(t)} = -\|\mathbf{z}^{(t)}\|_2^2$
- 10:   Backpropagate:  $\mathbf{a}^{(t+1)} = \mathbf{a}^{(t)} - \gamma \nabla \mathbf{a} \mathcal{L}^{(t)}$
- 11: **end for**
- 12: **Step 4: Quantitative evaluation**
- 13: Compute RE, NRMS and CC

in the spectral domain. Therefore, in the learnable compression scenario, the proposed model is not necessarily applicable to MPGFRFT-II.

We first test the learnable compression method on the first column of the SST dataset. A 5-NN symmetric graph is constructed to ensure the unitarity of the GFRFT and MPGFRFT-I. The compression ratio is set to  $r \in \{0.3, 0.5, 0.8\}$ , with a learning rate of 0.005, and a training duration of 1000 epochs. For initialization, the GFRFT order is set to  $\mathbf{a}_{\text{initial}} = 0.5$ , while the MPGFRFT methods use an initial order vector  $\mathbf{a}_{\text{initial}} = (0.5)_N$ . Table VI summarizes the compression performance of the learnable GFRFT, MPGFRFT-I, and MPGFRFT-II. As predicted by the theoretical anal-

TABLE VI  
LEARNABLE COMPRESSION PERFORMANCE ON SST DATASET.

RE/NRMS/CC	$r = 0.3$	$r = 0.5$	$r = 0.8$
GFRFT	7.26%/25.61%/97.06%	3.97%/13.03%/99.17%	4.05%/13.48%/99.26%
MPGFRFT-I	<b>6.64%/21.38%/97.89%</b>	<b>1.50%/5.23%/99.87%</b>	<b>0.00%/0.00%/100.00%</b>
MPGFRFT-II	201.30%/603.80%/71.59%	70.86%/218.83%/68.46%	13.67%/40.83%/95.62%

ysis above, the results confirm that the proposed learning framework is not suitable for MPGFRFT-II, likely due to its lack of unitarity, which breaks the energy preservation principle necessary for effective sparsity-based optimization. In contrast, learnable MPGFRFT-I consistently outperforms the single-parameter GFRFT across all compression ratios, demonstrating the advantage of a more expressive, multiple-parameter spectral basis under a unitary transform.

We further evaluate the method on a  $128 \times 128$  bottom-right patch of the rooftop image used in Section IV. The patch is divided into 256 non-overlapping  $8 \times 8$  blocks. Each block is flattened into a vector and compressed independently using the learnable framework. A symmetric 4-NN graph is constructed for each block. The compression ratio is set to  $r = 0.5$ , the learning rate is 0.005, and training is performed for 500 epochs per block. Fig. 4 presents the visual results of the reconstructed image blocks using learnable GFRFT, MPGFRFT-I, and MPGFRFT-II. As illustrated, the learnable MPGFRFT-I achieves the best visual quality, preserving structural details and introducing minimal artifacts. In contrast, GFRFT produces blurrier results with visible noise, and MPGFRFT-II yields severe distortion, aligning with earlier analysis of its limitations in this context. Quantitatively, the results are consistent with visual observations. MPGFRFT-I achieves RE = 2.04%, NRMS = 6.63%, and CC = 99.79%, significantly outperforming the single-parameter GFRFT (RE = 6.77%, NRMS = 20.52%, CC = 98.06%). MPGFRFT-II performs poorly, with RE = 58.97%, NRMS = 211.84%, and CC = 63.06%, further confirming its inadequacy under this framework.

#### D. Denoising

To evaluate the effectiveness of MPGFRFT in denoising tasks, we jointly learn the order vector and a diagonal filter in the spectral domain. The goal is to suppress noise while preserving signal structure by optimizing both the fractional transform and the filter response. The overall procedure is summarized in Algorithm 3.

1) *Real-Data Denoising*: Following the model setup described in Section V-B, we investigate the denoising performance of the proposed MPGFRFT framework on three real-world datasets: SST, PM-25, and COVID. For each dataset, we use the first two columns as clean reference signals and add Gaussian noise with varying noise levels  $\sigma \in \{0.2, 0.3, 0.4\}$ . We examine the denoising performance under different graph structures by varying the number of nearest neighbors  $k \in \{3, 6, 10\}$  in the  $k$ -NN graph construction.

For both MPGFRFT-I and MPGFRFT-II, we jointly learn the diagonal filter matrix  $\mathbf{H}$  and the transform order vector  $\mathbf{a}$ .

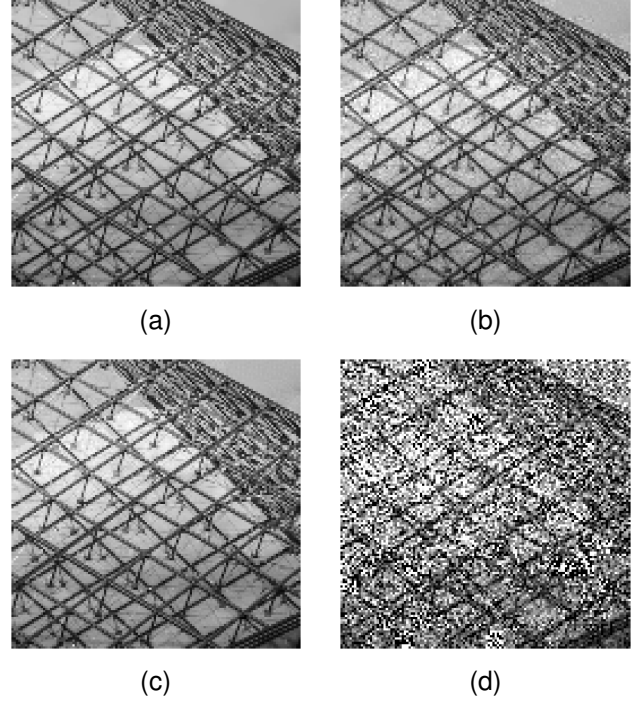


Fig. 4. Learnable compression results of rooftop image under 5-NN graph: (a) Original image; (b) Compressed image using learnable GFRFT; (c) Compressed image using learnable MPGFRFT-I; (d) Compressed image using learnable MPGFRFT-II.

---

#### Algorithm 3 Learnable Denoising using MPGFRFT

---

**Require:** Noisy signal  $\mathbf{y} \in \mathbb{R}^N$ , pure signal  $\mathbf{x}$ , learning rate  $\gamma$ , training epochs

**Ensure:** Optimized order vector  $\mathbf{a}_{\text{opt}}$ , diagonal filter  $\mathbf{H}_{\text{opt}}$ , SNR/MSE for real-data, and PSNR/MSE/SSIM for image

- 1: Initialize order vector  $\mathbf{a}_{\text{initial}} = (0.5)_N$ , diagonal filter  $\mathbf{H}_{\text{initial}} = \mathbf{I}_N$
  - 2: **for**  $t = 1$  to training epochs **do**
  - 3:   **Step 1: Operator construction**
  - 4:   Construct MPGFRFT matrix:  $(\mathbf{F}_a)^{(t)}$
  - 5:   **Step 2: Forward propagation**
  - 6:   Compute:  $\tilde{\mathbf{x}}^{(t)} = (\mathbf{F}_a^{(t)})^{-1} \mathbf{H}^{(t)} (\mathbf{F}_a^{(t)})^t \mathbf{y}$
  - 7:   **Step 3: Loss calculation and back propagation**
  - 8:   Compute loss:  $\mathcal{L}^{(t)} = \|\mathbf{z}^{(t)} - \mathbf{x}\|_2^2 / N$
  - 9:   Use Adam optimizer to update order vector  $\mathbf{a}^{(t+1)}$  and filter  $\mathbf{H}^{(t+1)}$
  - 10: **end for**
  - 11: **Step 4: Quantitative evaluation**
  - 12: Compute SNR/MSE for real-data, and PSNR/MSE/SSIM for image
-

TABLE VII  
DENOISING PERFORMANCE ON REAL-WORLD DATASETS (SST, PM-25, COVID) IN TERMS OF MSE AND SNR.

SST		$k = 3$			$k = 6$			$k = 10$		
		$\sigma = 0.2$	$\sigma = 0.3$	$\sigma = 0.4$	$\sigma = 0.2$	$\sigma = 0.3$	$\sigma = 0.4$	$\sigma = 0.2$	$\sigma = 0.3$	$\sigma = 0.4$
SNR	GFRFT	16.5083	13.5649	11.7268	16.2703	14.1556	12.4091	14.8912	11.6146	9.4403
	MPGFRFT-I	23.6505	21.9776	19.9185	25.7085	22.0223	21.0731	24.8787	22.1710	20.4976
	MPGFRFT-II	<b>27.9071</b>	<b>27.4889</b>	<b>24.3212</b>	<b>26.5261</b>	<b>28.0103</b>	<b>23.5948</b>	<b>32.2278</b>	<b>33.1109</b>	<b>29.2576</b>
MSE	GFRFT	$1.18 \times 10^{-2}$	$2.31 \times 10^{-2}$	$3.53 \times 10^{-2}$	$1.24 \times 10^{-2}$	$2.02 \times 10^{-2}$	$3.02 \times 10^{-2}$	$1.71 \times 10^{-2}$	$3.63 \times 10^{-2}$	$5.98 \times 10^{-2}$
	MPGFRFT-I	$2.27 \times 10^{-3}$	$3.34 \times 10^{-3}$	$5.36 \times 10^{-3}$	$1.41 \times 10^{-3}$	$3.30 \times 10^{-3}$	$4.11 \times 10^{-3}$	$1.71 \times 10^{-3}$	$3.19 \times 10^{-3}$	$4.69 \times 10^{-3}$
	MPGFRFT-II	<b><math>8.52 \times 10^{-4}</math></b>	<b><math>9.38 \times 10^{-4}</math></b>	<b><math>1.94 \times 10^{-3}</math></b>	<b><math>1.17 \times 10^{-3}</math></b>	<b><math>8.32 \times 10^{-4}</math></b>	<b><math>2.30 \times 10^{-3}</math></b>	<b><math>3.15 \times 10^{-4}</math></b>	<b><math>2.57 \times 10^{-4}</math></b>	<b><math>6.24 \times 10^{-4}</math></b>

PM-25		$k = 3$			$k = 6$			$k = 10$		
		$\sigma = 0.2$	$\sigma = 0.3$	$\sigma = 0.4$	$\sigma = 0.2$	$\sigma = 0.3$	$\sigma = 0.4$	$\sigma = 0.2$	$\sigma = 0.3$	$\sigma = 0.4$
SNR	GFRFT	6.5738	4.4782	3.9019	7.2241	6.1734	5.6800	7.3513	5.6900	5.0805
	MPGFRFT-I	16.8161	14.5545	13.4502	16.0280	15.9817	15.4266	15.9539	14.5063	16.3511
	MPGFRFT-II	<b>24.5476</b>	<b>22.5650</b>	<b>22.1658</b>	<b>23.0826</b>	<b>20.5501</b>	<b>19.7136</b>	<b>27.6770</b>	<b>24.2790</b>	<b>20.3433</b>
MSE	GFRFT	$7.44 \times 10^{-3}$	$1.20 \times 10^{-2}$	$1.38 \times 10^{-2}$	$6.40 \times 10^{-3}$	$8.15 \times 10^{-3}$	$9.13 \times 10^{-3}$	$6.22 \times 10^{-3}$	$9.11 \times 10^{-3}$	$1.05 \times 10^{-2}$
	MPGFRFT-I	$7.03 \times 10^{-4}$	$1.18 \times 10^{-3}$	$1.53 \times 10^{-3}$	$8.43 \times 10^{-4}$	$8.52 \times 10^{-4}$	$9.68 \times 10^{-4}$	$8.58 \times 10^{-4}$	$1.20 \times 10^{-3}$	$7.83 \times 10^{-4}$
	MPGFRFT-II	<b><math>1.19 \times 10^{-4}</math></b>	<b><math>1.87 \times 10^{-4}</math></b>	<b><math>2.05 \times 10^{-4}</math></b>	<b><math>1.66 \times 10^{-4}</math></b>	<b><math>2.98 \times 10^{-4}</math></b>	<b><math>3.61 \times 10^{-4}</math></b>	<b><math>5.77 \times 10^{-5}</math></b>	<b><math>1.26 \times 10^{-4}</math></b>	<b><math>3.12 \times 10^{-4}</math></b>

COVID		$k = 3$			$k = 6$			$k = 10$		
		$\sigma = 0.2$	$\sigma = 0.3$	$\sigma = 0.4$	$\sigma = 0.2$	$\sigma = 0.3$	$\sigma = 0.4$	$\sigma = 0.2$	$\sigma = 0.3$	$\sigma = 0.4$
SNR	GFRFT	5.5905	5.2322	4.9066	8.0647	6.3236	6.2418	6.8858	5.7942	4.8869
	MPGFRFT-I	17.5274	17.8199	15.0220	17.4098	15.1148	15.9522	16.1978	15.7910	15.2436
	MPGFRFT-II	<b>29.0094</b>	<b>24.6959</b>	<b>22.6331</b>	<b>28.9049</b>	<b>24.3216</b>	<b>25.9744</b>	<b>24.2843</b>	<b>21.8306</b>	<b>17.6633</b>
MSE	GFRFT	$2.79 \times 10^{-3}$	$3.03 \times 10^{-3}$	$3.27 \times 10^{-3}$	$1.58 \times 10^{-3}$	$2.36 \times 10^{-3}$	$2.40 \times 10^{-3}$	$2.07 \times 10^{-3}$	$2.66 \times 10^{-3}$	$3.28 \times 10^{-3}$
	MPGFRFT-I	$1.79 \times 10^{-4}$	$1.67 \times 10^{-4}$	$3.18 \times 10^{-4}$	$1.84 \times 10^{-4}$	$3.11 \times 10^{-4}$	$2.57 \times 10^{-4}$	$2.43 \times 10^{-4}$	$2.66 \times 10^{-4}$	$3.02 \times 10^{-4}$
	MPGFRFT-II	<b><math>1.27 \times 10^{-5}</math></b>	<b><math>3.43 \times 10^{-5}</math></b>	<b><math>5.51 \times 10^{-5}</math></b>	<b><math>1.30 \times 10^{-5}</math></b>	<b><math>3.74 \times 10^{-5}</math></b>	<b><math>2.55 \times 10^{-5}</math></b>	<b><math>3.77 \times 10^{-5}</math></b>	<b><math>6.63 \times 10^{-5}</math></b>	<b><math>1.73 \times 10^{-4}</math></b>

For comparison, the GFRFT-based method is also trained by jointly optimizing the filter  $\mathbf{H}$  and the scalar fractional order  $\alpha$ . To ensure computational efficiency, we retain only the first 100 nodes of the COVID dataset in all experiments. Table VII presents the denoising results in terms of both MSE and SNR across all datasets and experimental settings. The results show that the MPGFRFT-based methods consistently achieve lower MSE and higher SNR compared to the GFRFT-based approach. This indicates that learning both the transform and the filter jointly in the MPGFRFT framework leads to more effective noise suppression and signal recovery, regardless of the dataset, graph topology, or noise level.

2) *Image Denoising*: In this experiment, we evaluate the denoising performance of the proposed method using depth (Teddy [48] and Art [49]) and natural [50] (Cameraman, Baboon, Sailboat, Tiffany, Pepper) images. All input images are first resized to a uniform resolution of  $256 \times 256$  pixels. From each resized image, a region of size  $128 \times 128$  is directly extracted for denoising analysis. Additive white Gaussian noise is added to the extracted image patches to simulate a noisy environment. The noisy image is then divided into 256 non-overlapping blocks of size  $8 \times 8$ . Each block is reshaped into a vector and treated as an input signal. These signals are used independently to learn the filter coefficients and multiple fractional order parameters. For each block, a 4-NN graph is constructed based on the pixel coordinates, and the corresponding adjacency matrix is obtained. The learned parameters are subsequently applied to perform localized filtering on each block, and the denoised blocks are reassembled to reconstruct the image. To initialize the learning process, we set the initial order vector for the MPGFRFT-based method as  $\mathbf{a}_{\text{initial}} = (0.5)_N$ , where  $N$  denotes the number of nodes. For the GFRFT-based method, a initial order of  $a_{\text{initial}} = 0.5$  is adopted. These settings ensure a consistent starting point for

the optimization of fractional orders and filter parameters. The training is conducted for 300 epochs per block using a fixed learning rate of 0.005.

To quantitatively evaluate the denoising performance, we adopt the peak SNR (PSNR) as a metric. It is defined as

$$\text{PSNR} = 10 \log_{10} \left( \frac{255^2}{\text{MSE}} \right), \quad (62)$$

where a higher PSNR indicates better reconstruction quality. In addition to PSNR, we also employ the structural similarity index measure (SSIM) as a complementary metric for evaluating perceptual similarity. SSIM values range from 0 to 1, with values closer to 1 indicating better structural and visual consistency.

Table VIII presents the denoising performance in terms of PSNR, MSE, and SSIM on both depth and natural images. It can be observed that all three quantitative metrics consistently favor the GFRFT-based methods over the baselines. In particular, MPGFRFT-I achieves the highest PSNR and SSIM values while maintaining the lowest MSE across almost all images, demonstrating its strong capability in image denoising.

To provide a visual assessment of the denoising performance, Fig. 5 shows the results for four representative images: Teddy, Cameraman, Sailboat, and Pepper under the noise level  $\sigma = 40$ . Each row includes the clean image, the noisy observation, and the denoised outputs by three different methods. From the visual comparison, it is evident that the GFRFT-based method partially removes noise but still leaves noticeable residual artifacts. This can be attributed to the limitation of using a single fractional order parameter across the entire block, which reduces the flexibility of the transform. In contrast, the MPGFRFT-based methods produce significantly cleaner results with fewer noise remnants, further confirming their robustness and adaptability.



TABLE VIII  
DENOISING PERFORMANCE ON DEPTH (TEDDY, ART) AND NATURAL (CAMERAMAN, BABOON, SAILBOAT, TIFFANY, PEPPER) IMAGES IN TERMS OF PSNR, MSE AND SSIM.

Method	$\sigma = 20$			$\sigma = 30$			$\sigma = 40$		
	PSNR	MSE	SSIM	PSNR	MSE	SSIM	PSNR	MSE	SSIM
Teddy									
GFRFT	36.3878	$1.49 \times 10^1$	0.8616	29.3794	$7.50 \times 10^1$	0.6066	25.7347	$1.74 \times 10^2$	0.3951
MPGFRFT-I	<b>112.7171</b>	<b><math>3.48 \times 10^{-7}</math></b>	<b>1.0000</b>	<b>86.4501</b>	<b><math>1.47 \times 10^{-4}</math></b>	<b>1.0000</b>	<b>71.3169</b>	<b><math>4.80 \times 10^{-3}</math></b>	<b>0.9999</b>
MPGFRFT-II	73.0406	$3.23 \times 10^{-3}$	0.9999	55.0676	$2.02 \times 10^{-1}$	0.9970	46.8031	1.36	0.9806
Art									
GFRFT	40.6551	5.5921	0.9631	31.5731	45.27	0.8044	26.6299	$1.41 \times 10^2$	0.6317
MPGFRFT-I	<b>111.0485</b>	<b><math>5.11 \times 10^{-7}</math></b>	<b>1.0000</b>	<b>100.6904</b>	<b><math>5.55 \times 10^{-6}</math></b>	<b>1.0000</b>	<b>88.3831</b>	<b><math>9.44 \times 10^{-5}</math></b>	<b>1.0000</b>
MPGFRFT-II	91.3566	$4.76 \times 10^{-5}$	<b>1.0000</b>	70.3438	$0.60 \times 10^{-2}$	0.9999	56.1834	$1.57 \times 10^{-1}$	0.9983
Cameraman									
GFRFT	36.6192	$1.42 \times 10^1$	0.9191	33.0677	$3.21 \times 10^1$	0.8734	30.3389	$6.01 \times 10^1$	0.8093
MPGFRFT-I	<b>58.2605</b>	<b><math>9.71 \times 10^{-2}</math></b>	<b>0.9986</b>	<b>52.3684</b>	<b><math>3.77 \times 10^{-1}</math></b>	<b>0.9948</b>	<b>48.9415</b>	<b><math>8.30 \times 10^{-1}</math></b>	<b>0.9895</b>
MPGFRFT-II	47.6364	1.12	0.9855	42.6534	3.53	0.9591	39.6549	7.04	0.9311
Baboon									
GFRFT	38.2367	9.76	0.9879	31.9194	$4.18 \times 10^1$	0.9439	27.7172	$1.10 \times 10^2$	0.8571
MPGFRFT-I	<b>95.2338</b>	<b><math>1.95 \times 10^{-5}</math></b>	<b>1.0000</b>	<b>73.8511</b>	<b><math>2.68 \times 10^{-3}</math></b>	<b>1.0000</b>	<b>65.4927</b>	<b><math>1.84 \times 10^{-2}</math></b>	<b>0.9999</b>
MPGFRFT-II	65.9642	$1.65 \times 10^{-2}$	0.9999	55.7929	$1.71 \times 10^{-1}$	0.9997	47.9218	1.05	0.9983
Sailboat									
GFRFT	37.3976	$1.18 \times 10^1$	0.9703	31.6603	$4.44 \times 10^1$	0.9224	28.4056	$9.39 \times 10^1$	0.8546
MPGFRFT-I	<b>98.8568</b>	<b><math>8.46 \times 10^{-6}</math></b>	<b>1.0000</b>	<b>75.7252</b>	<b><math>1.74 \times 10^{-3}</math></b>	<b>0.9999</b>	<b>66.9183</b>	<b><math>1.32 \times 10^{-2}</math></b>	<b>0.9999</b>
MPGFRFT-II	70.7469	$5.48 \times 10^{-3}$	0.9999	56.0254	$1.62 \times 10^{-1}$	0.9993	50.1209	$6.32 \times 10^{-1}$	0.9977
Tiffany									
GFRFT	50.1066	$6.34 \times 10^{-1}$	0.9958	42.6431	3.54	0.9835	37.6761	$1.11 \times 10^1$	0.9582
MPGFRFT-I	<b>109.4183</b>	<b><math>7.43 \times 10^{-7}</math></b>	<b>1.0000</b>	<b>103.5487</b>	<b><math>2.87 \times 10^{-6}</math></b>	<b>1.0000</b>	<b>103.7303</b>	<b><math>2.75 \times 10^{-6}</math></b>	<b>1.0000</b>
MPGFRFT-II	102.9189	$3.32 \times 10^{-6}$	<b>1.0000</b>	95.8325	$1.70 \times 10^{-5}$	<b>1.0000</b>	98.6193	$8.94 \times 10^{-6}$	0.9999
Pepper									
GFRFT	39.7986	6.81	0.9823	33.1349	$3.16 \times 10^1$	0.9211	28.3398	$9.53 \times 10^1$	0.7793
MPGFRFT-I	<b>70.5177</b>	<b><math>5.77 \times 10^{-3}</math></b>	<b>0.9999</b>	<b>64.6178</b>	<b><math>2.25 \times 10^{-2}</math></b>	<b>0.9999</b>	<b>61.5568</b>	<b><math>4.54 \times 10^{-2}</math></b>	<b>0.9998</b>
MPGFRFT-II	57.1264	$1.26 \times 10^{-1}$	0.9995	53.1874	$3.12 \times 10^{-1}$	0.9988	48.4242	$9.35 \times 10^{-1}$	0.9969

### E. Image Encryption and Decryption

In this part, we develop a secure and effective image encryption-decryption framework that integrates chaotic DNA encoding with MPGFRFT-based spectral encryption. The detailed procedure is summarized in Algorithm 4.

If all keys and parameters are correctly used, the original image can be precisely recovered. To verify this, we apply the proposed MPGFRFT-based encryption and decryption schemes using a randomly sampled order vector  $\mathbf{a} \in \mathbb{R}^{64}$ , where each element is drawn from a uniform distribution in  $[0, 1]$ . Fig. 6 shows the results for both MPGFRFT-I and MPGFRFT-II schemes on the Airplane (F-16) image [51]. As can be seen, the image is perfectly restored when the correct multiple-parameter order vector is applied during decryption, validating the correctness of the proposed approach.

To quantitatively assess the statistical security of the encrypted images, we analyze the correlation of adjacent pixels in three directions: horizontal, vertical, and diagonal. The correlation is measured by randomly sampling 5,000 adjacent pixel pairs in each direction and computing the Pearson correlation coefficient. The correlation is calculated separately on each RGB channel and then averaged to obtain a single value per direction. In the original image, the correlation coefficients between adjacent pixels are notably high: 0.9674 in the horizontal direction, 0.9522 in the vertical direction, and 0.9300 in the diagonal direction. These values indicate strong spatial redundancy and smooth local variations, which are typical characteristics of natural images. After encryption using the MPGFRFT-I scheme, the corresponding correlation

coefficients drop significantly to  $-0.0116$ ,  $0.0043$ , and  $0.0003$ . For the MPGFRFT-II scheme, the correlation values are reduced to  $-0.0051$ ,  $0.0055$ , and  $-0.0018$ . These near-zero values suggest that the spatial dependencies among neighboring pixels have been effectively eliminated. This confirms the effectiveness of the proposed MPGFRFT-based encryption methods in resisting correlation-based cryptanalysis.

In practical encryption scenarios, slight deviations in key parameters may occur due to transmission noise or implementation imprecision. Therefore, it is essential to investigate the sensitivity of the encryption scheme to parameter perturbations. To this end, we study how small changes in the order vector affect the decryption quality, quantified by the MSE between the original and decrypted images. Both the GFRFT and the proposed MPGFRFT-I satisfy the property of index additivity, which ensures that their behaviors under parameter perturbation are theoretically consistent. As such, we focus our sensitivity analysis on the comparison between GFRFT and the proposed MPGFRFT-II. For the experiment, we set the encryption parameters of MPGFRFT-II as an order vector  $\mathbf{a} = (0.1, 0.3, 0.5, 0.8)_{16}$ , and use a single fractional order  $\alpha = 0.5$  for GFRFT. To evaluate sensitivity, we introduce an additive perturbation  $\delta$  to the decryption parameters, while keeping the encryption parameters fixed. The perturbation  $\delta$  is varied within the range  $\delta \in [-0.6, 0.6]$ . The resulting MSE values between the original and decrypted images under different  $\delta$  values are plotted in Fig. 7. As shown in Fig. 7, the MSE of both schemes increases as the absolute value of  $\delta$  grows, reflecting a decline in decryption



Fig. 5. Denoising results on Teddy, Cameraman, Sailboat, and Pepper images at noise level  $\sigma = 40$ .

accuracy due to parameter mismatch. Notably, under the same level of perturbation, the MSE of the MPGFRFT-II scheme fluctuates more significantly than that of the GFRFT scheme. This indicates that the MPGFRFT-II scheme exhibits higher sensitivity to parameter deviations. Such sensitivity, while requiring more precise control of decryption parameters, also implies enhanced security. The multiple-parameter design of MPGFRFT-II not only enlarges the key space, but also significantly increases decryption difficulty in the absence of precise key information, owing to its heightened sensitivity to parameter variations.

A major advantage of the multiple-parameter setting lies in the exponential expansion of the key space. In a conventional single-order GFRFT scheme with  $a \in [-2, 2]$  and a discretization step of 0.1, only 41 possible values exist. In contrast, the proposed MPGFRFT schemes adopt an order vector  $\mathbf{a} \in \mathbb{R}^N$ , where  $N$  is the number of nodes in each sub-region. This leads to a key space of size  $41^N$ , which increases exponentially with  $N$ . Furthermore, the spatial variation of keys further increases the complexity of decryption. To further demonstrate the increased security provided by the multiple-

parameter scheme, we attempt to decrypt the MPGFRFT-I encrypted image shown in Fig. 6(b) using all possible single-order GFRFT settings, with  $a \in [0.1, 1]$  and a step size of 0.1. Fig. 8 shows the decryption results obtained for each tested value of  $a$ . As shown in Fig. 8, some decrypted images using small values of  $a$  (e.g.,  $a = 0.1$  to 0.6) appear to partially reveal coarse color regions—such as the red parts of the airplane and the blue background resembling snow-covered mountains. However, these decrypted results fail to recover any structural details. Critical features such as the tail number, aircraft model, and even the overall shape of the airplane are entirely lost. Consequently, it remains impossible to recognize the object or infer any meaningful content. This demonstrates that single-order GFRFT fails to break the proposed multiple-parameter encryption scheme, even when limited visual resemblance is incidentally present.

## VI. CONCLUSION

In this paper, we proposed two types of MPGFRFTs to overcome the limitations of conventional GFRFT, which apply a single global fractional order across all graph frequencies. By introducing order vector, the MPGFRFT framework

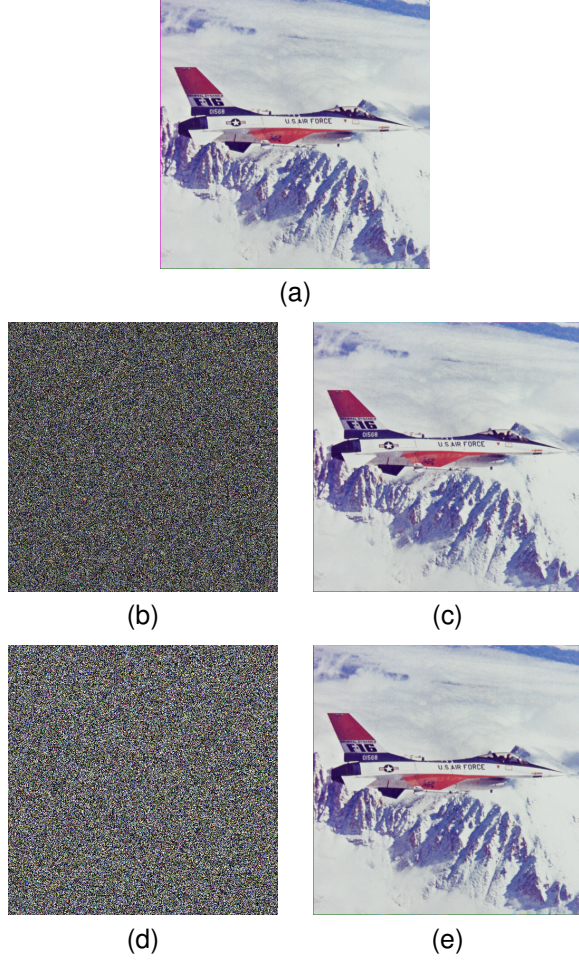


Fig. 6. Results of MPGFRFT-based encryption and decryption: (a) Original image; (b) Encrypted image using MPGFRFT-I; (c) Decrypted image using MPGFRFT-I; (d) Encrypted image using MPGFRFT-II; (e) Decrypted image using MPGFRFT-II.

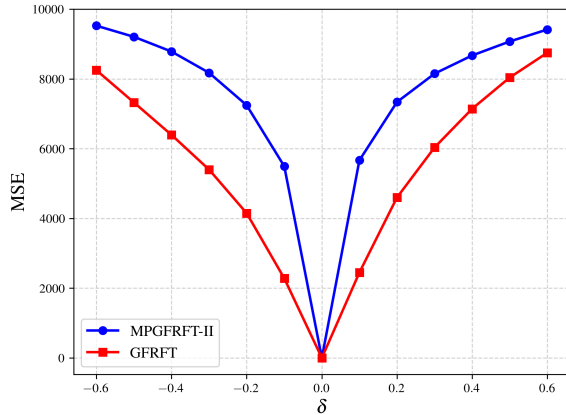


Fig. 7. Parameter sensitivity of the GFRFT and MPGFRFT-II.

---

#### Algorithm 4 Image Encryption and Decryption via DNA and MPGFRFT

---

**Require:** RGB image  $\mathbf{I} \in \mathbb{R}^{N \times N \times 3}$ , chaos parameters  $x_0, \eta$ , encryption order vector  $\mathbf{a}$ , decryption order vector  $\mathbf{b}$

**Ensure:** Reconstructed image  $\mathbf{I}_{\text{rec}}$

- 1: **Step 1: DNA-Based Encryption**
  - 2: **for** each channel  $c \in \{R, G, B\}$  **do**
  - 3:   Generate chaotic permutation  $\pi_c$  using logistic map  $(x_0, \eta)$
  - 4:   Permute pixels:  $\mathbf{I}_c^{\text{perm}} \leftarrow \mathbf{I}_c[\pi_c]$
  - 5:   DNA encode:  $\mathbf{D}_c \leftarrow \text{DNA\_encode}(\mathbf{I}_c^{\text{perm}})$  and generate chaotic mask  $\mathbf{M}_c$
  - 6:   Apply XOR in DNA domain  $\mathbf{X}_c \leftarrow \mathbf{D}_c \oplus \mathbf{M}_c$
  - 7:   Decode DNA to obtain encrypted channel  $\mathbf{I}_c^{\text{enc}}$
  - 8: **end for**
  - 9: Merge encrypted channels:  $\mathbf{I}_{\text{DNA}} \leftarrow \text{concat}(\mathbf{I}_R^{\text{enc}}, \mathbf{I}_G^{\text{enc}}, \mathbf{I}_B^{\text{enc}})$
  - 10: **Step 2: MPGFRFT-Based Spectral Encryption**
  - 11: Flatten  $\mathbf{I}_{\text{DNA}}$  and divide into groups via chaotic permutation
  - 12: **for** each group  $g_i$  **do**
  - 13:   Construct 4-NN graph and operator  $\mathbf{F}_i^{\mathbf{a}}$
  - 14:   Apply MPGFRFT:  $\hat{\mathbf{g}}_i^{\mathbf{a}} \leftarrow \mathbf{F}_i^{\mathbf{a}} g_i$
  - 15: **end for**
  - 16: Concatenate encrypted groups
  - 17: **Step 3: MPGFRFT-Based Decryption**
  - 18: **for** each encrypted group  $\hat{\mathbf{g}}_i^{\mathbf{a}}$  **do**
  - 19:   Apply inverse transform:  $\mathbf{g}_i' \leftarrow (\mathbf{F}_i^{\mathbf{b}})^{-1} \hat{\mathbf{g}}_i^{\mathbf{a}}$
  - 20: **end for**
  - 21: Concatenate all  $\mathbf{g}_i'$  to obtain  $\mathbf{I}_{\text{DNA}}^{\text{dec}}$
  - 22: **Step 4: DNA-Based Decryption**
  - 23: **for** each channel  $c \in \{R, G, B\}$  **do**
  - 24:   DNA encode:  $\tilde{\mathbf{D}}_c \leftarrow \text{DNA\_encode}(\mathbf{I}_c^{\text{dec}})$
  - 25:   XOR in DNA:  $\tilde{\mathbf{X}}_c \leftarrow \tilde{\mathbf{D}}_c \oplus \mathbf{M}_c$
  - 26:   Decode DNA:  $\mathbf{I}_c^{\text{perm}} \leftarrow \text{DNA\_decode}(\tilde{\mathbf{X}}_c)$
  - 27:   Inverse permutation:  $\mathbf{I}_{\text{rec},c} \leftarrow \mathbf{I}_c^{\text{perm}}[\pi_c^{-1}]$
  - 28: **end for**
  - 29: Merge channels:  $\mathbf{I}_{\text{rec}} \leftarrow \text{concat}(\mathbf{I}_{\text{rec},R}, \mathbf{I}_{\text{rec},G}, \mathbf{I}_{\text{rec},B})$
- 

achieves greater spectral adaptability and expressive power. We established the theoretical foundations of the proposed transforms and developed a learnable order vector scheme, enabling task-driven optimization in both synthetic and real-world settings. Furthermore, we designed a spectral compression strategy tailored for ultra-low compression ratios, which effectively preserves critical information even under extreme dimensionality reduction. To evaluate the practical value of the framework, we applied MPGFRFTs to a diverse range of tasks, including transform learning, order vector learning, compression, denoising, and image encryption and decryption. Experimental results consistently demonstrate the flexibility and effectiveness of the proposed MPGFRFT framework across various graph signal processing applications.

#### REFERENCES

- [1] A. Ortega, P. Frossard, J. Kovacevic, J. M. F. Moura, and P. Vandergheynst, "Graph signal processing: Overview, challenges, and applications," *Proc. IEEE*, vol. 106, no. 5, pp. 808–828, Apr. 2018.



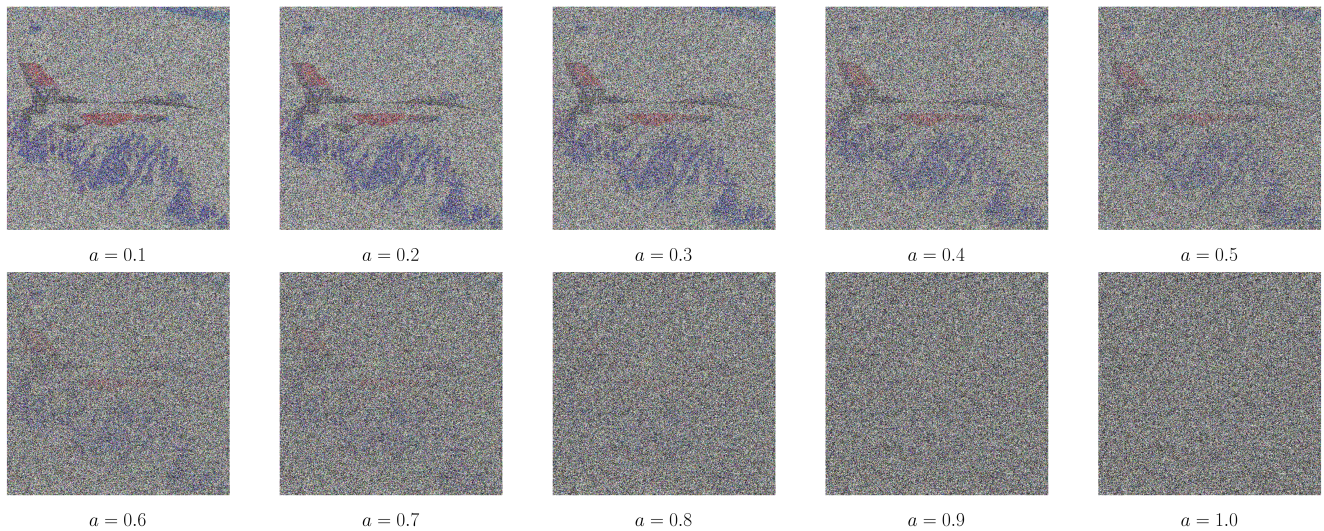


Fig. 8. Decryption results of the MPGFRFT-I encrypted image using single-order GFRFT with  $a \in [0, 1]$  and step size of 0.1.

- [2] A. Ortega, *Introduction to Graph Signal Processing*. Cambridge University Press, 2022.
- [3] G. Leus, A. G. Marques, J. M. Moura, A. Ortega, and D. I. Shuman, "Graph signal processing: History, development, impact, and outlook," *IEEE Signal Process. Mag.*, vol. 40, no. 4, pp. 49–60, Jun. 2023.
- [4] X. Y. Song, L. Chai, and J. X. Zhang, "Graph signal processing approach to QSAR/QSPR model learning of compounds," *IEEE Trans. Pattern Anal. Mach. Intell.*, vol. 44, no. 4, pp. 1963–1973, Oct. 2022.
- [5] R. Li, X. Yuan, M. Radfar, P. Marendy, W. Ni, T. J. O'Brien, and P. M. Casillas-Espinosa, "Graph signal processing, graph neural network and graph learning on biological data: A systematic review," *IEEE Rev. Biomed. Eng.*, vol. 16, pp. 109–135, Dec. 2023.
- [6] S. S. Saboksayr, G. Mateos, and M. Cetin, "EEG-based emotion classification using graph signal processing," in *Proc. IEEE International Conference on Acoustics, Speech and Signal Processing (ICASSP)*, Jun. 2021, pp. 1065–1069.
- [7] A. Gavili and X. P. Zhang, "On the shift operator, graph frequency, and optimal filtering in graph signal processing," *IEEE Trans. Signal Process.*, vol. 65, no. 23, pp. 6303–6318, 2017.
- [8] A. Sandryhaila and J. M. F. Moura, "Discrete signal processing on graphs," *IEEE Trans. Signal Process.*, vol. 61, no. 7, pp. 1644–1656, Jan. 2013.
- [9] G. G. Dong, H. W. Liu, G. Y. Kuang, and J. Chanussot, "Target recognition in SAR images via sparse representation in the frequency domain," *Pattern Recognit.*, vol. 96, p. 106972, Dec. 2019.
- [10] J. L. Wang, R. Gao, H. T. Zheng, H. Zhu, and C.-J. R. Shi, "SSGCNet: A sparse spectra graph convolutional network for epileptic EEG signal classification," *IEEE Trans. Neural Netw. Learn. Syst.*, vol. 35, no. 9, pp. 12 157–12 171, Mar. 2024.
- [11] X. Y. Song, K. Wu, and L. Chai, "Brain network analysis of schizophrenia patients based on hypergraph signal processing," *IEEE Trans. Image Process.*, vol. 32, pp. 4964–4976, Aug. 2023.
- [12] Q. Bao, B. Gang, W. Yang, J. Zhou, and Q. Liao, "Attention-driven graph neural network for deep face super-resolution," *IEEE Trans. Image Process.*, vol. 31, pp. 6455–6470, Oct. 2022.
- [13] K.-S. Lu and A. Ortega, "Fast graph Fourier transforms based on graph symmetry and bipartition," *IEEE Trans. Signal Process.*, vol. 67, no. 18, pp. 4855–4869, Aug. 2019.
- [14] J. Domingos and J. M. F. Moura, "Graph Fourier transform: A stable approximation," *IEEE Trans. Signal Process.*, vol. 68, pp. 4422–4437, Jul. 2020.
- [15] G. Patane, "Fourier-based and rational graph filters for spectral processing," *IEEE Trans. Pattern Anal. Mach. Intell.*, vol. 45, no. 6, pp. 7063–7074, May 2023.
- [16] W. F. Qi, S. R. Guo, and W. Hu, "Generic reversible visible watermarking via regularized graph Fourier transform coding," *IEEE Trans. Image Process.*, vol. 31, pp. 691–705, Dec. 2022.
- [17] S. Bochner and K. Chandrasekharan, *Fourier Transforms*. Princeton: Princeton University Press, 1949.
- [18] H. J. Nussbaumer and H. J. Nussbaumer, *The Fast Fourier Transform*. Berlin: Springer, 1982.
- [19] B. Girault, P. Goncalves, and E. Fleury, "Translation on graphs: An isometric shift operator," *IEEE Signal Process. Lett.*, vol. 22, no. 12, pp. 2416–2420, Oct. 2015.
- [20] F. Ji, W. P. Tay, and A. Ortega, "Graph signal processing over a probability space of shift operators," *IEEE Trans. Signal Process.*, vol. 71, pp. 1159–1174, Mar. 2023.
- [21] E. Isufi, F. Gama, and A. Ribeiro, "Edgenets: Edge varying graph neural networks," *IEEE Trans. Pattern Anal. Mach. Intell.*, vol. 44, no. 11, pp. 7457–7473, Sep. 2022.
- [22] Y. F. Liu and B. Du, "Frequency domain-oriented complex graph neural networks for graph classification," *IEEE Trans. Neural Netw. Learn. Syst.*, vol. 36, no. 2, pp. 2733–2746, Feb. 2025.
- [23] F. Xia, K. Sun, S. Yu, A. Aziz, L. Wan, S. Pan, and H. Liu, "Graph learning: A survey," *IEEE Trans. Artif. Intell.*, vol. 2, no. 2, pp. 109–127, Apr. 2021.
- [24] N. Q. Li, W. J. Li, Y. H. Gao, Y. M. Li, J. G. Bao, E. E. Kuruoglu, Y. Jiang, and S. T. Xia, "Node-level graph regression with deep Gaussian process models," *IEEE Trans. Artif. Intell.*, vol. 5, no. 6, pp. 3257–3269, Jun. 2024.
- [25] Y. Q. Wang and B. Z. Li, "The fractional Fourier transform on graphs: Sampling and recovery," in *Proc. 14th IEEE International Conference on Signal Processing (ICSP)*, Aug. 2018, pp. 1103–1108.
- [26] W. Pan, K. H. Qin, and Y. Chen, "An adaptable-multilayer fractional Fourier transform approach for image registration," *IEEE Trans. Pattern Anal. Mach. Intell.*, vol. 31, no. 3, pp. 400–414, Apr. 2009.
- [27] X. D. Zhao, M. M. Zhang, R. Tao, W. Li, W. Z. Liao, L. F. Tian, and W. Philips, "Fractional Fourier image transformer for multimodal remote sensing data classification," *IEEE Trans. Neural Netw. Learn. Syst.*, vol. 35, no. 2, pp. 2314–2326, Feb. 2024.
- [28] C. Ozturk, H. M. Ozaktas, S. Gezici, and A. Koç, "Optimal fractional Fourier filtering for graph signals," *IEEE Trans. Signal Process.*, vol. 69, pp. 2902–2912, May 2021.
- [29] F. J. Yan and B. Z. Li, "Windowed fractional Fourier transform on graphs: Properties and fast algorithm," *Digit. Signal Process.*, vol. 118, p. 103210, Nov. 2021.
- [30] Y. C. Gan, J. Y. Chen, and B. Z. Li, "The windowed two-dimensional graph fractional Fourier transform," *Digit. Signal Process.*, vol. 162, p. 105191, Jul 2025.
- [31] T. Alikasifoglu, B. Kartal, and A. Koc, "Wiener filtering in joint time-vertex fractional Fourier domains," *IEEE Signal Process. Lett.*, vol. 31, pp. 1319–1323, May 2024.
- [32] T. Alikasifoglu, B. Kartal, E. Ozgunay, and A. Koc, "Joint time-vertex fractional Fourier transform," *Signal Process.*, vol. 233, p. 109944, Aug. 2025.
- [33] T. Alikasifoglu, B. Kartal, and A. Koc, "Graph fractional Fourier transform: A unified theory," *IEEE Trans. Signal Process.*, vol. 72, pp. 3834–3850, Aug. 2024.

- [34] J. Y. Chen, Y. Zhang, and B. Z. Li, "Graph linear canonical transform: Definition, vertex-frequency analysis and filter design," *IEEE Trans. Signal Process.*, vol. 72, pp. 5691–5707, Dec. 2024.
- [35] E. Isufi, F. Gama, D. I. Shuman, and S. Segarra, "Graph filters for signal processing and machine learning on graphs," *IEEE Transactions on Signal Processing*, vol. 72, pp. 4745–4781, Jan. 2024.
- [36] F. J. Yan and B. Z. Li, "Multi-dimensional graph fractional Fourier transform and its application to data compression," *Digit. Signal Process.*, vol. 129, p. 103683, Sep. 2022.
- [37] N. Li and Z. C. Zhang, "Multi-dimensional graph linear canonical transform," *Digit. Signal Process.*, vol. 165, p. 105334, Oct. 2025.
- [38] F. M. Bianchi, D. Grattarola, L. Livi, and C. Alippi, "Graph neural networks with convolutional ARMA filters," *IEEE Trans. Pattern Anal. Mach. Intell.*, vol. 44, no. 7, pp. 3496–3507, Jan. 2022.
- [39] A. Salim and S. Sumitra, "Spectral graph convolutional neural networks in the context of regularization theory," *IEEE Trans. Neural Netw. Learn. Syst.*, vol. 35, no. 4, pp. 4373–4384, Jun. 2024.
- [40] R. Airani and S. Kambale, "Spectral approximation of Gaussian random graph laplacians and applications to pattern recognition," *Pattern Recognit.*, vol. 164, p. 111555, Aug. 2025.
- [41] S. C. Pei and W. L. Hsue, "The multiple-parameter discrete fractional Fourier transform," *IEEE Signal Process. Lett.*, vol. 13, no. 6, pp. 329–332, Jun. 2006.
- [42] X. J. Kang, R. Tao, and F. Zhang, "Multiple-parameter discrete fractional transform and its applications," *IEEE Trans. Signal Process.*, vol. 64, no. 13, pp. 3402–3417, Mar. 2016.
- [43] Y. Q. Wang, B. Z. Li, and Q. Y. Cheng, "The fractional Fourier transform on graphs," in *Proc. Asia-Pacific Signal and Information Processing Association Annual Summit and Conference (APSIPA ASC)*, Dec. 2017, pp. 105–110.
- [44] A. G. Marques, S. Segarra, G. Leus, and A. Ribeiro, "Sampling of graph signals with successive local aggregations," *IEEE Trans. Signal Process.*, vol. 64, no. 7, pp. 1832–1843, Dec. 2016.
- [45] X. H. Wang, J. X. Chen, and Y. T. Gu, "Local measurement and reconstruction for noisy bandlimited graph signals," *Signal Process.*, vol. 129, pp. 119–129, Dec. 2016.
- [46] H. Sheng, H. Feng, J. H. Yu, F. Ji, and B. Hu, "Sampling theory of jointly bandlimited time–vertex graph signals," *Signal Process.*, vol. 222, p. 109522, Sep. 2024.
- [47] J. Giraldo, A. Mahmood, B. Garcia-Garcia, D. Thanou, and T. Bouwmans, "Reconstruction of time-varying graph signals via Sobolev smoothness," *IEEE Trans. Signal Inf. Process. Netw.*, vol. 8, pp. 201–214, Mar. 2022.
- [48] D. Scharstein and R. Szeliski, "High-accuracy stereo depth maps using structured light," in *Proc. IEEE Computer Society Conference on Computer Vision and Pattern Recognition (CVPR 2003)*, Jul. 2003, p. 1.
- [49] D. Scharstein and C. Pal, "Learning conditional random fields for stereo," in *Proc. IEEE Computer Society Conference on Computer Vision and Pattern Recognition (CVPR 2007)*, Jul. 2007, pp. 1–8.
- [50] <https://gitcode.com/Premium-Resources/75708>.
- [51] <https://sipi.usc.edu/database/database.php?volume=misc&image=11>.

**Zhichao Zhang** (Member, IEEE) received the B.S. degree in mathematics and applied mathematics from Gannan Normal University, Ganzhou, Jiangxi, China, in 2012, and the Ph.D. degree in mathematics of uncertainty processing from Sichuan University, Chengdu, Sichuan, China, in 2018. From September 2017 to September 2018, he was a Visiting Student Researcher with the Department of Electrical and Computer Engineering, Tandon School of Engineering, New York University, Brooklyn, NY, USA, where he was awarded a grant from the China Scholarship Council. From January 2021 to January 2023, he was a Macau Young Scholars Post-Doctoral Fellow of information and communication engineering with the School of Computer Science and Engineering, Macau University of Science and Technology, Macau, SAR, China. Since 2019, he has been with the School of Mathematics and Statistics, Nanjing University of Information Science and Technology, Nanjing, Jiangsu, China, where he is currently a Full Professor and a Doctoral Supervisor. He has published more than 60 journal articles in IEEE TRANSACTIONS ON INFORMATION THEORY, IEEE TRANSACTIONS ON SIGNAL PROCESSING, IEEE SIGNAL PROCESSING LETTERS, IEEE COMMUNICATIONS LETTERS, Signal Processing, and Journal of Fourier Analysis and Applications. His current research interests include mathematical theories, methods, and applications in signal and information processing, including fundamental theories, such as Fourier analysis, functional analysis and harmonic analysis, applied theories, such as signal representation, sampling, reconstruction, filter, separation, detection and estimation, and engineering technologies, such as satellite communications, radar detection, and electronic countermeasures. He was the Vice President of the Jiangsu Society for Computational Mathematics; the Director of the Jiangsu Society for Industrial and Applied Mathematics; and a member of the International Association of Engineers, the China Society for Industrial and Applied Mathematics, the Chinese Institute of Electronics, and the Beijing Society for Interdisciplinary Science. He was listed among world's top 2% scientists recognized by Stanford University in 2021 and 2022.

**Wei Yao** received the B.S. and M.S. degrees in pure mathematics from Shaanxi Normal University, Xi'an, China, in 2002 and 2005, respectively, and the Ph.D. degree in applied mathematics from Beijing Institute of Technology, Beijing, China, in 2008. He is currently a Professor with Nanjing University of Information Science and Technology, Nanjing, China.

**Manjun Cui** received the B.S. degree in Mathematics and Applied Mathematics from Yancheng Teachers University, Yancheng, Jiangsu, China, in 2022. She is currently pursuing the Ph.D. degree in mathematics with the School of Mathematics and Statistics, Nanjing University of Information Science and Technology, Nanjing, Jiangsu, China.